Sheared sheet intrusions as mechanism for lateral flank displacement on basaltic volcanoes: Applications to Réunion Island volcanoes

Valérie Cayol, Thibault Catry, Laurent Michon, Marie Chaput, Vincent Famin, Olivier Bodart, Jean-Luc Froger, C. Romagnoli

AGU PUBLICATIONS

JGR

Journal of Geophysical Research: Solid Earth

RESEARCH ARTICLE
10.1002/2014JB011139

Key Points:
- Sheared sheet intrusions are the most efficient slip surface
- At Piton des Neiges, a pile of sills accommodated ~200 m of flank displacement
- A decision tree is provided to infer fracture characteristics from displacements

Supporting Information:
- Readme
- Figure S1
- Figure S2
- Figure S3
- Figure S4
- Figure S5
- Figure S6
- Figure S7
- Figure S8
- Figure S9
- Figure S10
- Figure S11
- Figure S12
- Figure S13
- Figure S14
- Figure S15
- Figure S16
- Figure S17
- Figure S18
- Figure S19
- Figure S20

Correspondence to:
V. Cayol,
v.cayol@opgc.fr

Citation:
Cayol, V., T. Catry, L. Michon, M. Chaput, V. Famin, O. Bodart, J.-L. Froger, and C. Romagnoli (2014), Sheared sheet intrusions as mechanism for lateral flank displacement on basaltic volcanoes: Applications to Réunion Island volcanoes, *J. Geophys. Res. Solid Earth*, *119*, 7607–7635, doi:10.1002/2014JB011139.

Received 28 MAR 2014
Accepted 17 SEP 2014
Accepted article online 24 SEP 2014
Published online 30 OCT 2014

Sheared sheet intrusions as mechanism for lateral flank displacement on basaltic volcanoes: Applications to Réunion Island volcanoes

V. Cayol[1,2], T. Catry[3,4], L. Michon[3], M. Chaput[3], V. Famin[3], O. Bodart[1,2,5], J.-L. Froger[1], and C. Romagnoli[4]

[1]Laboratoire Magmas et Volcans, UMR 6524, CNRS-IRD-Université Blaise Pascal, Clermont-Ferrand, France, [2]Université Jean Monnet, Université de Lyon, St Etienne, France, [3]Laboratoire GéoSciences Réunion, Institut de Physique de Paris, Université de la Réunion, Saint-Denis, France, [4]Dipartimento di Scienze Biologiche, Geologiche ed Ambientali, Università di Bologna, Bologna, Italy, [5]Laboratoire de Mathématiques, UMR 6620, CNRS-Université Blaise Pascal, Aubière CEDEX, France

Abstract Field work carried out on the Piton des Neiges volcano (Réunion Island) suggests that the injection of magma along detachments could trigger flank failure by conjugate opening and shear displacement. We use 3-D numerical models to compare the ability of purely opened sheet intrusions, sheared sheet intrusions, and normal faults to induce flank displacement on basaltic volcanoes. We assume that shear stress change on fractures results from stress anisotropy of the host rock under gravity. Exploring a large range of stress anisotropies, fracture dips, and fracture depth over length ratios, we determine that the amount of shear displacement is independent of the proximity to the ground surface. Sheared sheet intrusions are the most efficient slip medium on volcanoes. Consequently, the largest flank displacement is induced by the longest, deepest sheared intrusion dipping closest to 45° in a host rock with the highest stress anisotropy. Using our model in a forward way, we provide shear and normal displacements for buried fractures. Applying the model to a pile of sills at the Piton des Neiges volcano, we determine that the mean shear displacement caused by each intrusion was 3.7 m, leading to a total of a 180–260 m of lateral displacement for the 50 m high pile of sills. Using our model in an inverse way, we formulate a decision tree to determine some fracture characteristics and the host rock stress anisotropy from ratios of maximum surface displacements. This procedure provides a priori models, which can be used to bound the parameter space before it is explored through a formal inversion. Applying the decision tree to the 1.4 m coeruptive flank displacement recorded at Piton de la Fournaise in 2007, we find that it probably originated from a shallow eastward dipping subhorizontal normal fault.

1. Introduction

Lateral flank collapse is one of the main causes of destruction of oceanic basaltic volcanoes [*Holcomb and Searle*, 1991]. The consequences of such processes, i.e debris avalanches [*Moore et al*., 1989] and tsunamis [*Keating and McGuire*, 2000; *Kelfoun et al*., 2010], make this issue of primary importance for risk mitigation.

Flank movements can be driven by gravity alone, the edifice being affected by spreading [*Borgia et al*., 1992; *Merle and Borgia*, 1996; *van Wyk de Vries and Francis*, 1997], or by the combined effects of gravity and forceful magma injections [*Swanson et al*., 1976; *Borgia*, 1994; *Lundgren et al*., 2004]. Forceful magma injection models assume that the volcano flank slides on a low angle fault, pushed by the recurrent injection of magma into vertical rift zones [*Dieterich*, 1988]. Frictional resistance of the fault can be reduced by pore fluid pressure [*Thomas et al*., 2004]. However, suprahydrostatic fluid pressure is required to explain the occurrence of catastrophic failures [*Iverson*, 1995; *Elsworth and Day*, 1999]. Such pressure can be reached for unrealistically thick clay layers (several hundred of meters) or in the case of extremely low hydraulic diffusivity [*Iverson*, 1995]. Another mechanism involves earthquake shaking, which induces ground liquefaction through elevated pore fluid pressure, possibly enhanced by gases [*Papatheodorou and Ferentinos*, 1997; *Thomas et al*., 2004], but this mechanism only concerns the shallow subsurface. Thus, the origin of large-scale flank failure remains enigmatic.

An alternative cause of large-scale flank failure has recently been proposed following field work on Piton des Neiges [*Famin and Michon*, 2010], the deeply incised extinct volcano of Réunion Island in the Indian

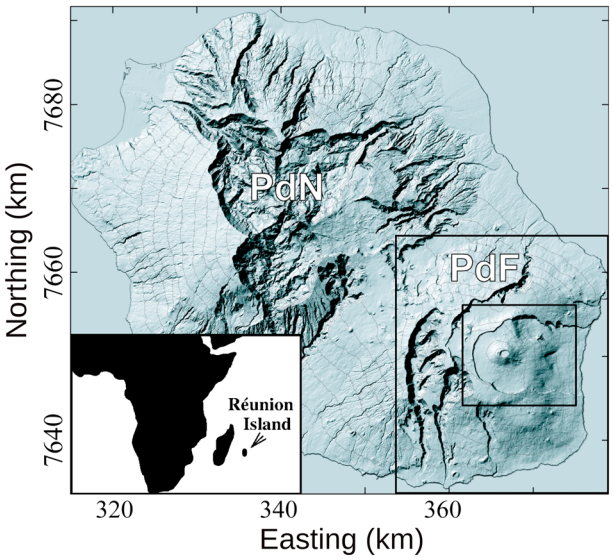

Figure 1. Location of Piton des Neiges and Piton de la Fournaise volcanoes. The large box outlines the slope map shown in Figure 12, and the small box marks the area of the displacement map shown in Figure 15. The coordinates correspond to UTM WGS84 (zone 40S). The inset shows the location of Réunion Island.

Ocean (Figure 1). The injection of magma along a detachment (i.e., a low-angle normal fault) leads to shearing of the emplaced sheet intrusion, which enhances the lateral displacement of the edifice flanks. A previous study [*Delaney et al*., 1986] recognized the existence of sheared sheet intrusions and investigated the conditions under which fracture orientation and shear displacement could be used to infer the host rock stress. Our study extends their investigation to the failure ability of a variety of fractures, including sheet intrusions, which can be purely opened (formed in mode I) or sheared (modes I + II), and faults (formed in mode II) located beneath prominent volcanoes having different stress anisotropies such that the tectonic context is extensional. Our study is complementary to the study of *Chaput et al*. [2014a] that explores the conditions required for magma injection along a detachment to promote fault slip and lead to edifice collapse.

In April 2007, Piton de la Fournaise, the active volcano of Réunion Island, experienced a large-scale (1.4 m) seaward displacement coeval with an eruption. This displacement was recorded by interferometric synthetic aperture radar (InSAR). One question raised by this displacement field and the study of the neighboring analog volcano, Piton des Neiges, is whether it is possible to distinguish surface displacements resulting from a sheet intrusion (sheared or not) from those resulting from a fault. Another question is whether the dip of the fracture, as well as the host rock stress field can be characterized by simple rules of thumb, generalizing the approach developed by *Pollard et al*. [1983] for purely opened subvertical sheet intrusions to a variety of fracture modes and fracture dips. Such an approach could guide further formal inversions by providing a priori models, which can be used to bound the explored parameter space.

The purpose of this paper is twofold. First, we investigate the amount of fracture displacement, surface displacement, and slope change that sheet intrusions (sheared or not) and faults can trigger on basaltic volcanoes. We also discuss the possibility of sheared intrusions triggering large-scale flank failures. Second, we design a step-by-step procedure to assess fracture and host rock stress characteristics from surface displacements associated with sheet intrusions and faults.

We first review the most common intrusion dips encountered on basaltic volcanoes. This section gives inputs for the numerical modeling of fracture, host rock, surface displacement, and slope variation related to sheet intrusions and faults of different orientations, under different stress fields. Second, we discuss our results and apply them to assess the shear displacement of some subhorizontal intrusions observed at Piton des Neiges. We also apply our results to the study of the slopes of basaltic shield volcanoes and to the determination of the fracture and host rock anisotropy corresponding to the flank displacement of the April 2007 Piton de la Fournaise eruption.

2. Sheet Intrusions Within Basaltic Edifices

Several field analyses were conducted on active and extinct basaltic shield volcanoes in order to characterize the geometry of the magmatic plumbing systems. Studies at Koolau volcano (Oahu Island, Hawaii) [*Walker*, 1986], Waianae volcano (Oahu Izsland, Hawaii) [*Zbinden and Sinton*, 1988], Tutulia volcano (American Samoa) [*Walker and Eyre*, 1995], Tenerife (Canary Islands) [*Marinoni and Gudmundsson*, 2000], Stromboli [*Tibaldi*, 2003], and Piton de la Fournaise (Réunion Island) [*Letourneur et al*., 2008] have shown that steeply dipping (subvertical) sheet intrusions (>60°) account for most of the plumbing system as they

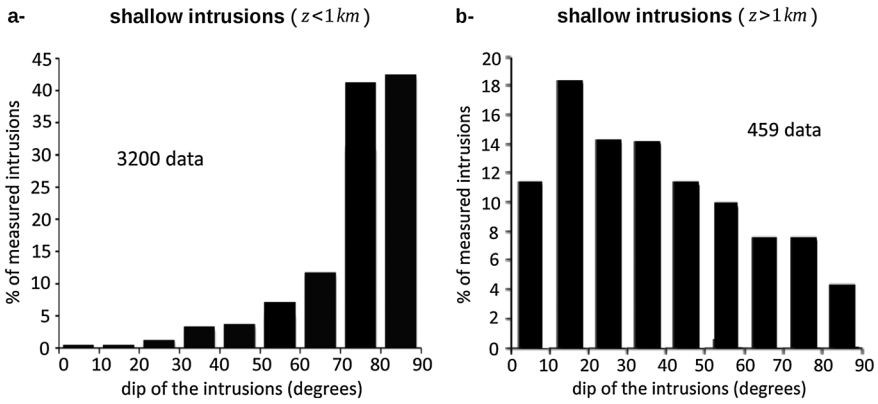

Figure 2. Orientations of sheet intrusions as a function of depth. (a) Dips of 3200 sheet intrusions measured at poorly eroded basaltic volcanoes (depth $<$ 1 km) [*Walker*, 1986; *Zbinden and Sinton*, 1988; *Walker and Eyre*, 1995; *Marinoni and Gudmundsson*, 2000; *Tibaldi*, 2003; *Letourneur et al*., 2008]. (b) Dips of 459 sheet intrusions measured in the deeply eroded Piton des Neiges volcano (depth $>$ 1 km).

represent 85% of all intrusions (Figure 2a). These subvertical intrusions are observed in the upper structural level of the edifice, at a maximum depth of about 1 km.

Very different dips have been described for the intrusive complexes injected into the lowermost units of the volcanic edifices of La Gomera and La Palma Islands (Canary Islands), and at the Piton des Neiges volcano, where the cores of the volcanoes outcrop. At La Gomera, most sheet intrusions are made up of outward (i.e., seaward) low-dipping (subhorizontal) sheet intrusions ($<$30°) [*Cendrero*, 1970; *Ancochea et al*., 2008]. Similarly, at La Palma, abundant subhorizontal intrusions cut the submarine sequence of the edifice, above the basal plutonic complex [*Staudigel and Schmincke*, 1984; *Fernández et al*., 2002]. Detailed studies of these volcanoes [*Ancochea et al*., 2008; *Staudigel and Schmincke*, 1984] show that intrusions emplaced in the older deeper part of the edifices are subhorizontal, while those observed in the shallower younger units are subvertical. The subhorizontal intrusions are frequently cut by dikes related to the younger edifice. At the Piton des Neiges volcano, abundant subhorizontal intrusions are also observed in the lower edifice [*Chevallier and Vatin-Perignon*, 1982; *Famin and Michon*, 2010].

To quantitatively confirm this observation, we carried out field analysis of the southern part of Piton des Neiges. Our data indicate that 43% of the intrusions in the inner part (depth $\geq$ 1 km) of the Piton des Neiges volcano have dips $<$30° and only 20% of the intrusions have dips $>$60° (Figure 2b). Magma injections at Piton des Neiges are therefore dominated by subhorizontal intrusions.

3. Numerical Modeling of Fractures

3.1. Model Description

In this work we use a mixed boundary element numerical method (MBEM) [*Cayol and Cornet*, 1997] to study the response of a volcano to subvertical and subhorizontal fractures and to establish rules of thumb for discriminating between displacement fields associated with sheet intrusions (sheared or not) and faults. The MBEM is a fully three-dimensional method, which considers realistic topographies and any number and geometry of sources (magma reservoirs, sheet intrusions, or faults) for media that are linearly elastic, homogeneous, and have isotropic rock properties. The precision and applicability of the MBEM for modeling volcanic deformation processes have already been tested [*Cayol and Cornet*, 1997; *Fukushima et al*., 2005] and applied to several volcanoes such as Piton de la Fournaise [*Cayol and Cornet*, 1998; *Froger et al*., 2004; *Fukushima et al*., 2010; *Peltier et al*., 2007, 2008], Merapi volcano [*Beauducel and Cornet*, 1999], Kilauea volcano [*Cayol et al*., 2000; *Dieterich et al*., 2000], and several Japanese volcanoes [*Takada and Fukushima*, 2013]. Here the boundary element method is modified in order to avoid fracture interpenetration when required (see Appendix A).

Our model is static, as we are interested in the final deformation produced by fractures. Boundary conditions are stress vectors, with the stress vector normal to the ground surface being null. Three different types of

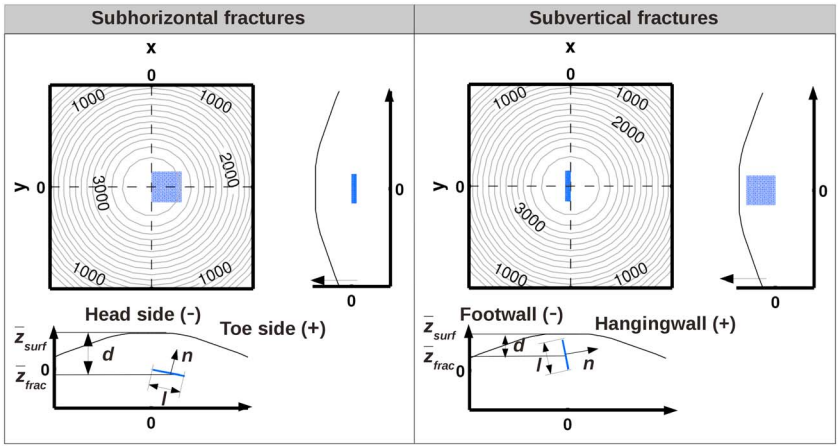

Figure 3. Geometries of subhorizontal (subh) and subvertical (subv) fractures considered in the model. The ***n*** is the unit vector normal to the fracture, $\bar{z}_{surf}$ is the mean elevation of the surface above the fracture, $\bar{z}_{frac}$ is the mean elevation of the fracture, and *l* is the fracture length. The $d = (\bar{z}_{surf} - \bar{z}_{frac})$ is the mean depth of the fracture beneath the surface. The contour lines are drawn at 200 m intervals, and the volcano summit is at $z = 3700$ m.

fractures are considered, corresponding to different stress changes on the fracture: (i) Purely opened sheet intrusions are fractures that open as a response to the driving pressure when magma pressure exceeds the host rock stress assumed to result from gravity. This is the typical load considered for intrusions in the literature [*Anderson*, 1938; *Pollard and Holzhausen*, 1979; *Jaeger et al*., 2009]. (ii) Sheared sheet intrusions are fractures which deform as a response to coeval driving pressure and full relaxation of host rock shear stress. The magma cancels friction and allows for full relaxation of the shear stress, which is acting when sheet intrusions are not emplaced perpendicular to a principal stress. This typically occurs when the intrusion direction is guided by a preexisting fracture [*Delaney et al*., 1986; *Maccaferri et al*., 2011], by a rheological contrast [*Kavanagh et al*., 2006; *Menand*, 2008; *Maccaferri et al*., 2011], or if an intrusion, while propagating in a medium with an heterogeneous stress field, does not fully reorient itself in response to a rotation of the host rock stress [*Dahm*, 2000; *Watanabe et al*., 2002; *Menand*, 2011; *Maccaferri et al*., 2011]. (iii) Faults are fractures deforming as a response to shear stress changes. We assume that fault friction is zero so that faults, in the same way as intrusions, fully relax the host rock stress. In our models, stress changes on fractures result from depth-dependent magma pressure and host rock stress, but for simplicity, a mean value is considered. In contrast to another recent study on the shear displacement of sills [*Chaput et al*., 2014a], we assume that when magma is involved, the whole fracture surface is subject to magmatic pressure. The boundary element code solves for the displacement distribution that matches the stress boundary conditions, resulting in variable displacement even when the fracture is submitted to a constant stress change.

We use geographical coordinates for which the *z* axis is vertical, and the *x* and *y* axes are oriented east-west and north-south, respectively (Figure 3). The topography and fractures are meshed by triangular elements. Mesh density is high in areas where deformation gradients are expected to be greatest and decreases away from these areas (see Figure S1 in the supporting information). In order to avoid edge effects, the mesh dimension is taken to be 5 times the largest fracture dimension [*Cayol*, 1996].

Slopes of basaltic volcanoes usually range from a few degrees to 12° [*Rowland and Garbeil*, 2000], although some volcanic edifices, like Piton de la Fournaise and the volcanoes of the Galapagos Islands, have unusually steep slopes reaching 20° to 35° locally. An axially symmetrical cone-shaped topography with 20° slopes is thus considered as our reference topography (Figure 3).

3.2. Fracture Geometry and Location

The strike of the intrusions is chosen to be north-south (Figure 3). Because the 3-D extent of fractures is difficult to constrain in the field, we assume that subvertical and subhorizontal fractures are planar and have a simple square shape (Figure 3). Following our compilation of field data, subvertical fractures are assumed to have dips, α, ranging from 60° to 90°, and subhorizontal fractures are assumed to have dips ranging from 0 to 30°.

Table 1. Parameters (Figure 3) and Physical Properties Used in the Calculation

Parameter or Property	Symbol
Geometrical Parameters	
Mean elevation of the surface above the fracture	z_{surf}
Mean elevation of the fracture	z_{frac}
Fracture length	l
Fracture mean depth	$d = z_{surf} - z_{frac}$
Physical Properties	
Horizontal and vertical stresses	σ_h, σ_v
Ratio of effective stresses	$k = \sigma_h/\sigma_v$
Crust friction coefficient	μ
Young's Modulus	E
Poisson's ration	ν
Fracture dip	α
Rock density	ρ_r
Magma density	ρ_m
Magma pressure	P_m
Normal stress change	$\Delta\sigma_n$
Shear stress change	$\Delta\tau$
Lithospheric pressure	P_{lith}

Fractures are assumed to originate at 3–4 km depth beneath the volcano summit, corresponding to the level of neutral buoyancy in basaltic edifices (i.e., the level where magma density equals the density of the surrounding rock) [*Tilling and Dvorak*, 1993]. This depth corresponds to the presumed depth of the shallowest reservoir at Kilauea [*Cervelli and Miklius*, 2003], Krafla [*Tryggvason*, 1986], and Piton de la Fournaise [*Prôno et al*., 2009; *Di Muro et al*., 2014]. This is also the estimated depth of emplacement for the subhorizontal intrusions at Piton des Neiges [*Famin and Michon*, 2010]. In our models, the top of the subhorizontal fractures and the bottom of the subvertical ones are located at $z = 0$, beneath the axis of symmetry of the topography, corresponding to $x = 0$ (Figure 3). Fractures have sides of length, $l = 3$ km (see Table 1 for the definitions of the main symbols). Under this hypothesis, the fracture depth over length ratio, d/l, has a mean value of $d/l = 0.8$ for subvertical fractures, whereas the mean value is $d/l = 1.4$ for subhorizontal fractures.

3.3. Stress in the Edifice

Initial stress in the volcano is assumed to be such that, at the location of intrusion, the maximum principal stress is vertical. Indeed, this stress field is consistent with the occurrence of flank spreading and with the direction of the maximum principal stress computed from gravity-loaded models which is subvertical, except for the shallowest part of the edifice where it becomes parallel to the ground surface [*Dieterich*, 1988; *Cayol and Cornet*, 1998; *Currenti and Williams*, 2014]. Following these models, we assume that the intermediate and minimum principal stresses are subequal along the intrusion. These hypotheses are consistent with the inversion of fault slip data at Piton des Neiges, which showed that the dominant stress field is extensional and the intermediate and minimum principal stress are subequal [*Chaput et al*., 2014b]. The principal stresses will be referred to as σ_v and σ_h for the vertical and horizontal principal stresses, respectively.

In order to quantify the stress anisotropy in the edifice, we define the stress ratio k as

$$k = \frac{\sigma_h}{\sigma_v}. \tag{1}$$

As we are looking at intraplate shield volcanoes, it is assumed that the regional stress has little influence on the stress field in the edifice; thus, there is no compression and $k \leq 1$.

A crude estimate of the crust stress ratio k is given by considering a half-space deforming uniaxially under its own weight (no horizontal deformation). For this special case, the stress ratio is

$$k = \frac{\nu}{(1-\nu)} = \frac{1}{3}, \tag{2}$$

for a Poisson's ratio $\nu = 0.25$ [*Jaeger et al*., 2009].

Several pieces of evidence indicate that the successive loading episodes undergone by the crust lead to a state of failure equilibrium. Both in volcanic islands and the continental crust, earthquakes are triggered by stress changes resulting from fault movements [*Stein et al*., 1992; *Segall et al*., 2006] or from fluid movement, whether magmatic [*Dieterich et al*., 2000], aqueous [*Roeloffs*, 1996], or gaseous [*Segall et al*., 1994].

In situ stress measurements in deep wells and boreholes worldwide [*Townend and Zoback*, 2000] show that the Coulomb failure theory fits the measurements of friction coefficients μ in the range of 0.6 to 1. These studies also indicate that pore pressure is close to hydrostatic. Assuming that the crust is in a state of failure equilibrium, we determine that k, for a fluid saturated crust, is given by

$$k = \frac{\sqrt{1+\mu^2}-\mu}{\sqrt{1+\mu^2}+\mu} + 2\frac{\rho_w}{\rho_r}\frac{\mu}{\sqrt{1+\mu^2}+\mu}, \tag{3}$$

where ρ_w and ρ_r are the density of water and the bulk density of volcanic rocks, respectively. Taking $\rho_r = 2700\ \mathrm{kg/m^3}$ and considering friction coefficients corresponding to the range of values determined in laboratory experiments ($\mu = 0.6$ to 1), we get a narrow range of k values from 0.5 to 0.6.

The values of $k > 0.6$ could occur for rocks that are not at the rock strength limit. For instance, $k = 1$ corresponds to a lithostatic state of stress, which might be found on volcanoes subjected to repeated dike injections [*Dieterich*, 1988]. This state of stress is consistent with the successive intrusion of radial and circumferential dikes on the Galapagos Islands [*Chadwick and Dieterich*, 1995]. It was also determined from the modeling of surface displacement and eruptive fissure opening at Réunion Island [*Cayol and Cornet*, 1998], where it is also consistent with a lack of seismicity at the shallow depths where dikes are emplaced [*Fukushima et al.*, 2010].

In order for our study to be comprehensive, we have explored displacements induced by fractures within edifices with stress ratios of $0.5 \le k \le 1$, where $k = 0.5$ and $k = 1$ correspond to rocks at the rock strength limit and at the lithostatic limit, respectively. The smaller the k value, the greater the stress anisotropy and the deviatoric stress (difference between the stress tensor and the mean stress).

3.4. Applied Stress Perturbation

For fractures at angle, α, we consider a mean shear stress change, $\Delta\tau$ (see Appendix B),

$$\Delta\tau = \rho_r g d \frac{(k-1)}{2} \sin(2\alpha), \tag{4}$$

where d is the mean fracture depth below the ground surface (Figure 3) and g is the acceleration of gravity.

For sheet intrusions (sheared or not), the mean driving pressure, $\Delta\sigma_n$, corresponding to the difference between the magma pressure and the host rock stress normal to the fracture, is assumed to have values between 1 and 10 MPa. Indeed, driving pressures determined from the inversion of geodetic data on basaltic shield volcanoes like Piton de la Fournaise [*Peltier et al.*, 2007, 2008; *Fukushima et al.*, 2010] or Sierra Negra volcano (Galapagos) [*Yun et al.*, 2006], range from 0 to a few megapascal. We assume that the magma pressure is greater than the magnitude of the maximum principal stress of the host rock so that fractures of any orientation can dilate.

The three types of fractures tested in the present work are characterized by the following stress conditions:

1. Purely opened sheet intrusions: Fractures are submitted to a driving pressure, $\Delta\sigma_n$. This stress change is met when the stress ratio $k = 1$, or when the intrusion is perpendicular to σ_h or σ_v, which is the case here for horizontal or vertical fractures, respectively. We assume that an intrusion can be emplaced perpendicular to σ_v, a case which might occur if the intrusion follows a preexisting fracture or a rheological contrast.
2. Sheared sheet intrusions: Fractures are submitted to a mixed loading corresponding to a driving pressure, $\Delta\sigma_n$, combined with a shear stress change, $\Delta\tau$. This load is met when the stress field is anisotropic ($k < 1$) and the intrusion is not perpendicular to a principal stress. As for purely opened intrusions, $\Delta\sigma_n$ is assumed to range from 1 to 10 MPa, and as for faults, $\Delta\tau$ is given by equation (4).
3. Normal faults: Fractures are only submitted to a shear stress change $\Delta\tau$ induced by an extensional stress field. On the fracture $\Delta\sigma_n$ is zero, and $\Delta\tau$ is given by equation (4).

3.5. Scaling of the Results

In order to be able to generalize our results to any stress, elastic parameter, or fracture dimension, the shear U_s and normal U_n (opening) fracture displacements are scaled by the shear U_s^{inf} and normal U_n^{inf}

displacements induced by shear $\Delta\tau$ and normal $\Delta\sigma_n$ stress changes on a circular fracture embedded in an infinite medium (see Appendix C for derivation). Thus,

$$[U_s] = U_s^{\inf} = \frac{32}{3\pi}\frac{(1-\nu^2)}{E(2-\nu)}\frac{l}{\sqrt{(\pi)}}\Delta\tau, \tag{5}$$

and

$$[U_n] = U_n^{\inf} = \frac{16}{3\pi}\frac{(1-\nu^2)}{E}\frac{l}{\sqrt{(\pi)}}\Delta\sigma_n, \tag{6}$$

where E is the Young's modulus and $l/\sqrt{(\pi)}$ is the radius of a circular source with the same area as the square source of side l considered in this study.

As we want the displacement to be independent of the applied lithostatic stress, shear stress changes are scaled by the lithostatic pressure

$$[\Delta\tau] = P_{\text{lith}} = \rho_r g d. \tag{7}$$

Internal and surface displacements are scaled by the mean displacement across a circular fracture in an infinite space:

$$[U] = \frac{16}{3\pi}\frac{(1-\nu^2)}{E}\frac{l}{\sqrt{(\pi)}}\sqrt{\Delta\sigma_n^2 + \frac{4}{(2-\nu)^2}\Delta\tau^2}, \tag{8}$$

where $\Delta\tau$ is given by equation (4).

Finally, distances are scaled by the mean depth of the fracture below the ground surface, d (Figure 3)

$$[d] = d = (\bar{z}_{surf} - \bar{z}_{frac}). \tag{9}$$

The ground surface has extra characteristic scales, which correspond to the radius of the summit area where the ground surface is flat and to the mean slope. These characteristic scales are not taken into account in the normalization. When fractures are buried as in our study, *Currenti et al*. [2008] showed that the mean slope has a second-order effect. Therefore, we expect the results to depend to the second order, on the mean slope, and the fracture length and depth.

In the subsequent sections, we investigate the joint influence of the stress anisotropy, fracture dip, and ground surface on the edifice deformation by computing fracture stress changes, fracture displacements, and surface displacements for three types of fractures, i.e., purely opened intrusions, sheared intrusions, and faults. The influence of $\Delta\sigma_n$ is also studied for sheared intrusions. For purely opened intrusions $\Delta\sigma_n$ is not specified. Displacement is a linear function of $\Delta\sigma_n$, and since it has been scaled by $\Delta\sigma_n$, it does not depend on it.

4. Fracture Stress and Displacement Ratio

In this section, we study fracture stress and displacement as a function of the fracture dip and the host rock stress ratio. We compare stress and displacement with values determined for circular fractures in an infinite medium, and we determine a simple way to calculate them where 3-D numerical models are lacking.

As we only discuss mean values, we will refer to mean stress or mean displacement simply as stress or displacement, respectively. Using the scaling previously defined, we study the dimensionless shear stress change $\Delta\tau^* = \Delta\tau/[P]$, the ratio of dimensionless shear over normal displacement $U_s^*/U_n^* = U_s/U_n * [U_n]/[U_s]$, the dimensionless shear displacement $U_s^* = U_s/[U_s]$, and opening $U_n^* = U_n/[U_n]$ (Figure 4).

As determined from equation (4), $\Delta\tau^* = (k-1)\sin(2\alpha)/2$ linearly decreases as k increases, becoming zero for $k = 1$ (Figure 4a). It varies the same as the dip of subhorizontal fractures and inversely to the dip of subvertical fractures. Parameter $\Delta\tau^*$ is the maximum for $\alpha = 45°$ and $k = 0.5$.

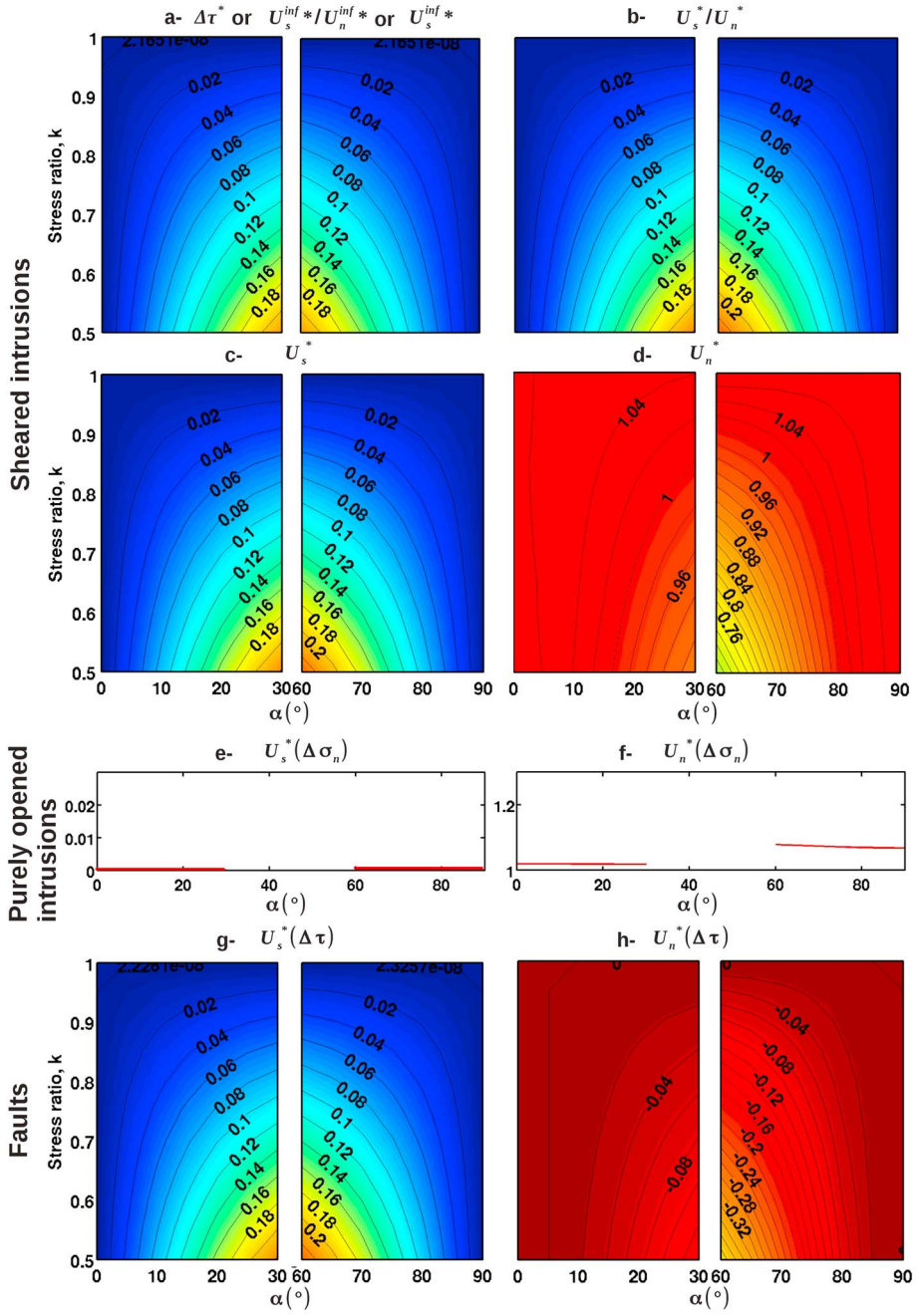

Figure 4. Influence of the dip, α, and stress ratio, k, on the fracture stress and displacement ratio for fractures of length $l = 3$ km. Here $U_s^* = U_s/[U_s]$, $U_n^* = U_n/[U_n]$, where scaling factors $[U_s]$ and $[U_n]$ are given by equations (5) and (6). (a) Dimensionless shear stress change, $\Delta\tau^*$, applied to subhorizontal and subvertical sheared intrusions as a function of α and k, $\Delta\tau^* = U_s^{inf\,*}/U_n^{inf\,*} = U_s^{inf\,*}$. (b) Ratio of dimensionless shear displacement over opening, U_s^*/U_n^*. (c, e, and g) Dimensionless opening U_n^*. Scaling is such that $U_n^{inf\,*} = 1$. (d, f, and h) Dimensionless shear displacement U_s^*. Interpenetration of fractures is permitted here, leading to negative openings on faults.

In linear elasticity, the superposition principle holds, and the displacement is a linear function of the applied stress change,

$$U_f = U_f(\Delta\tau + \Delta\sigma_n) = U_f(\Delta\tau) + U_f(\Delta\sigma_n) = P_{\text{lith}} U_f(\Delta\tau^*) + \Delta\sigma_n U_f(1), \tag{10}$$

where the subscript f stands for the shear ($f = s$) or normal ($f = n$) directions to the fracture, respectively. For circular fractures in an infinite medium, $U_n(\Delta\tau) = 0$ and $U_s(\Delta\sigma_n) = 0$ (equations (5) and (6)), so that $U_s^{\text{inf}}/U_n^{\text{inf}}$

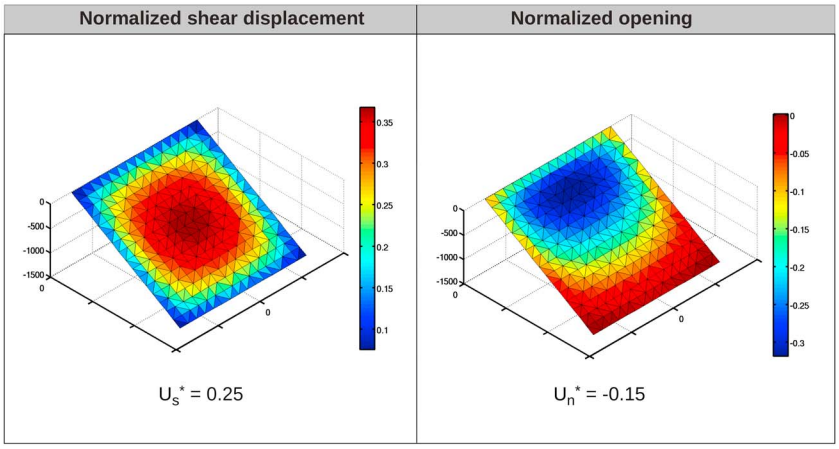

Figure 5. Normalized displacement obtained for a 30° dip fault, for which fracture wall interpenetration is not prevented. The fault is located beneath a ground surface sloping at 20°. U_s* and U_n* are the mean shear displacement and opening of the sheared intrusion, respectively.

is a linear function of $\Delta\tau/\Delta\sigma_n$. Because of the chosen normalization, the ratio of the dimensionless shear displacement over the opening of the sheared circular fractures in an infinite medium U_s^{inf*}/U_n^{inf*} (equations (5) and (6)) simply equals the dimensionless shear stress,

$$\frac{U_s^{inf*}}{U_n^{inf*}} = \Delta\tau^* = \frac{(k-1)}{2}\sin(2\alpha). \tag{11}$$

For square sheared fractures within a three-dimensional volcano, we determine that U_s*/U_n* (Figure 4b) is close to predictions for a circular fracture in an infinite medium U_s^{inf*}/U_n^{inf*} (Figure 4a), U_s*/U_n* ~ $\Delta\tau$* where fractures are subhorizontal or subvertical with $\alpha > 80°$ and $k > 0.8$. For these fractures, U_s*/U_n* is thus independent of the fracture area, which indicates that like circular fractures in a infinite medium, U_s* and U_n* are linear functions of this area. For subvertical fractures with $\alpha < 80°$ and $k < 0.8$, U_s*/U_n* is greater than U_s^{inf*}/U_n^{inf*}, resulting from a decrease of the opening, U_n*, with the dip (Figure 4d). The inspection of the terms contributing to U_n* in equation (10), i.e., U_n*($\Delta\sigma_n$) (Figure 4f) and U_n*($\Delta\tau$) (Figure 4h), indicates that the decrease of U_n* is induced by negative U_n*($\Delta\tau$) occurring on the upper part of the fracture (Figure 5).

Negative U_n*($\Delta\tau$) corresponds to fracture wall interpenetration, a result which is mathematically correct, but unlikely to actually occur in basalt. Under a mixed stress change, the negative U_n*($\Delta\tau$) results in a smaller opening than would occur if the medium was infinite (see equation (10)). To ensure that fracture interpenetration does not occur, it will be prevented in the rest of the paper (Appendix A).

Studying the influence of the ground surface on displacement and displacement ratios, we find that U_s* is not very sensitive to the proximity of the ground surface: $U_s^* = U_s^{inf*} = \Delta\tau^*$ regardless of d/l (Figure S3 in the supporting information). However, the opening, U_n*, is strongly increased or decreased by the vicinity of the ground surface: the shallower the sheared fracture (or the smaller d/l), the greater the deviation of U_n* from $U_n^{inf*} = 1$, the opening of a circular purely opened fracture in an infinite medium (Figure S4 in the supporting information). The deviations of U_n* from $U_n^{inf*} = 1$ occur as soon as $d/l < 1.2$ for subhorizontal fractures, or $d/l < 2$ for subvertical fractures. For intermediate dips $30° < \alpha < 80°$, U_n* is smaller than in an infinite medium ($U_n^* < U_n^{inf*} = 1$), whereas U_n* is greater ($U_n^* > U_n^{inf*} = 1$) for fractures closer to the horizontal and, to a smaller extent, vertical directions. This value can be up to 4 times greater than U_n^{inf*} for subhorizontal fractures close to the ground surface where $d/l < 0.6$ and $\alpha \approx 0°$. Similarly, when k is small, sheared intrusions undergo less opening than for greater k values, and purely opened intrusions ($k = 1$). In other words, at shallow depth, the occurrence of shear displacement induces fracture closure.

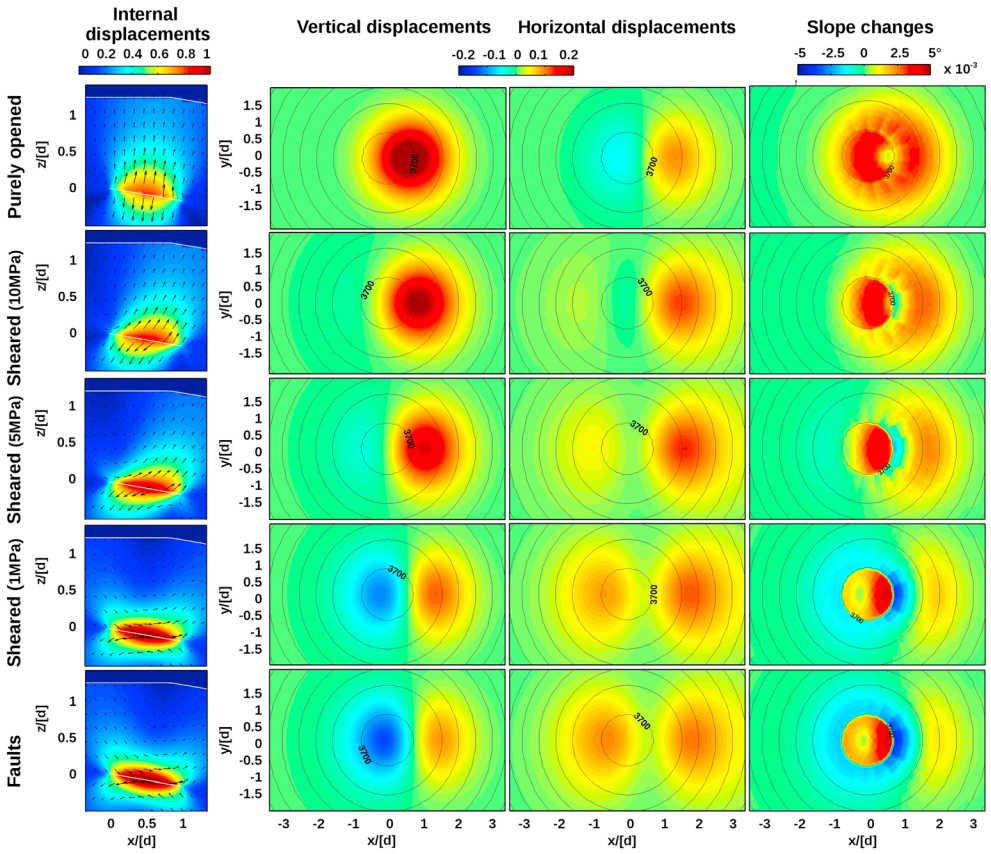

Figure 6. Dimensionless internal displacement, surface displacement, and slope changes associated with different types of subhorizontal fractures ($\alpha = 10°$): purely opened sheet intrusions (driving pressure $\Delta\sigma_n$), sheared sheet intrusions (mixed stress change corresponding to a combination of driving pressure $\Delta\sigma_n$ and shear stress change $\Delta\tau$ with $k = 0.6$), and faults (shear stress change, $\Delta\tau$ with $k = 0.6$). Displacement and slope changes are scaled by $[U]$ given by equation (8). The contour lines indicate the ground surface elevations. They are every 500 m.

Finally, using $[U_s]$, $[U_n]$, and $[\tau]$, given in equations (5)–(7), we determine that for deep subhorizontal fractures such that $d/l \geq 1.2$ or subvertical fractures such that $d/l \geq 2$, displacement and displacement ratios can be approximated by those of circular fractures in an infinite medium:

$U_s = U_s^{\inf}$, where $U_s^{\inf}$ is given by equation (5) with $\Delta\tau$ given by equation (4),

$$U_s = \frac{32}{3\pi}\frac{(1-\nu^2)}{E(2-\nu)}\frac{l}{\sqrt{(\pi)}}\frac{(k-1)}{2}\sin(2\alpha)\rho_r g d, \tag{12}$$

$U_n = U_n^{\inf}$, where $U_n^{\inf}$ is given by equation (6),

$$U_n = \frac{16}{3\pi}\frac{(1-\nu^2)}{E}\frac{l}{\sqrt{(\pi)}}\Delta\sigma_n. \tag{13}$$

and

$$\frac{U_s}{U_n} = \frac{U_s^{\inf}}{U_n^{\inf}} = \frac{2}{(2-\nu)}\frac{\Delta\tau}{\Delta\sigma_n} = \frac{2}{(2-\nu)}\frac{(k-1)}{2}\sin(2\alpha)\frac{\rho_r g d}{\Delta\sigma_n}. \tag{14}$$

For shallow subhorizontal fractures where $d/l < 1.2$ or shallow subvertical fractures where $d/l < 2$, curves specific to d/l given in Figures S4 and S2 in the supporting information should be used to compute U_n and U_s/U_n, respectively, using

$$U_n = \frac{16}{3\pi}\frac{(1-\nu^2)}{E}\frac{l}{2}\Delta\sigma_n\left(U_n^*\right)_{\text{curves}}, \tag{15}$$

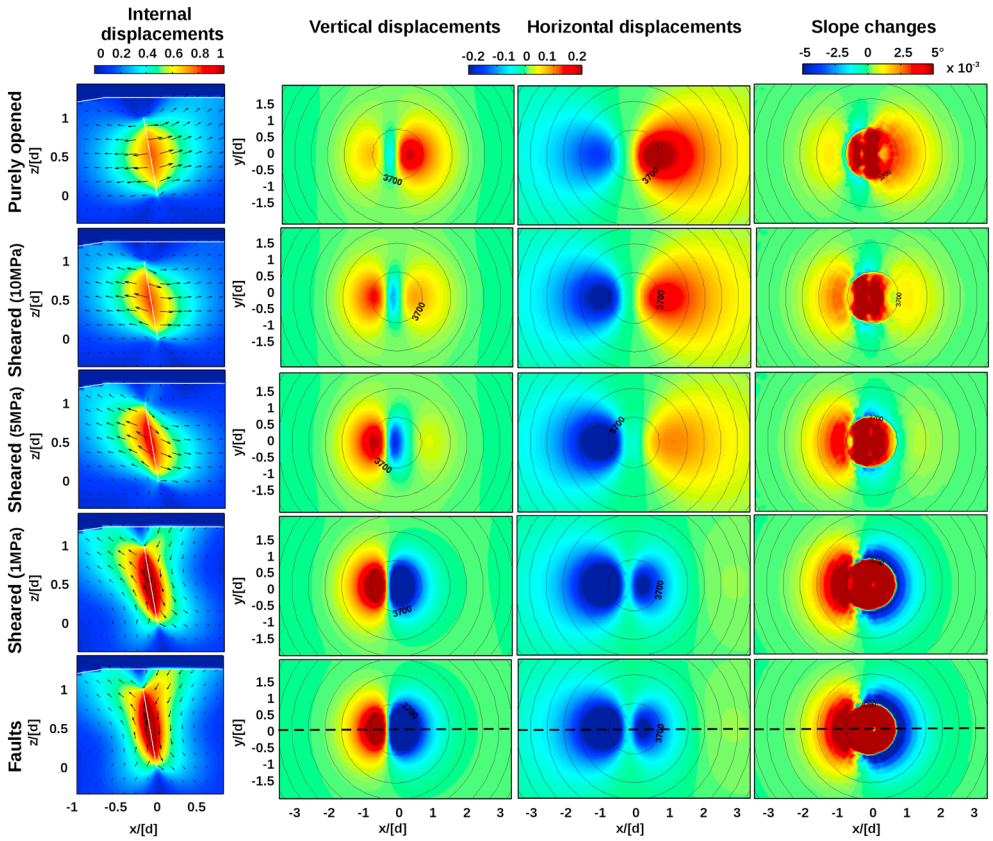

Figure 7. Same as previous figure but for subvertical fractures (α = 80°).

and

$$\frac{U_s}{U_n} = \frac{2}{(2-\nu)} \frac{\rho_f g d}{\Delta\sigma_n} \left(\frac{U_s^*}{U_n^*}\right)_{\text{curves}}, \tag{16}$$

while $U_s = U_s^{\text{inf}}$ is given by equation (12) above.

Conversely, these equations and curves can be used to infer the driving pressure and lithostatic stress from the observed fracture displacement.

5. Surface Displacement and Slope Change

We describe the dimensionless displacement and slope change for (i) a subhorizontal fracture with a 10° dip and (ii) a subvertical fracture with an 80° dip for the three different loading cases. The displacement and slope are scaled by $[U]$ given in equation (8). A stress ratio of $k = 1$ is chosen for purely opened intrusions, and $k = 0.6$ is chosen for sheared intrusions and faults. Based on this, ratios of maximum displacements are defined to infer fracture and host rock characteristics from the observed fracture displacement.

For subhorizontal fractures, the head of the fracture will be referred to as side "−" and the toe of the fracture as side "+" (Figure 3a), while for subvertical fractures, the foot side will be referred to as side "−" and the hanging side as side "+" (Figure 3b).

Because the displacement of sheared intrusions are the weighted sum of displacement created by faults and purely opened intrusions (equation (10)), a continuum of displacement is observed (Figures 6 and 7) from purely opened intrusions (driving pressure, $\Delta\sigma_n \neq 0$ MPa and $\Delta\tau = 0$ MPa) to sheared intrusions (mixed stress change, $\Delta\sigma_n \neq 0$ MPa and $\Delta\tau \neq 0$ MPa) and, with decreasing driving pressure, to the final stage corresponding to faults (shear stress change $\Delta\tau \neq 0$ MPa and $\Delta\sigma_n = 0$ MPa).

5.1. Subhorizontal Fracture (α = 10°)

Purely opened intrusions and sheared intrusions with large $\Delta\sigma_n$ (5 MPa) have large internal uplift above the fracture (Figure 6). The smaller $\Delta\sigma_n$, the smaller this uplift. For sheared intrusions with $\Delta\sigma_n = 1$ MPa and faults, uplift is lowest above the fracture center and greater toward the edges. Purely opened intrusions and sheared intrusions with large $\Delta\sigma_n$ show westward internal displacement above the head of the intrusion and eastward displacement above the toe, whereas sheared intrusions with $\Delta\sigma_n = 1$ MPa and faults have eastward displacement above the fracture and westward displacement below.

At the ground surface, these displacements result in unimodal uplifts for purely opened and sheared intrusions with large $\Delta\sigma_n$, and in opposite vertical displacement at the head side, which subsides, and the toe side, which is uplifted, for sheared intrusions with $\Delta\sigma_n = 1$ MPa and faults. Horizontal surface displacement points in opposite directions, westward on the head side and eastward on the toe side, for purely opened intrusions and sheared intrusions with large $\Delta\sigma_n$, while it points eastward on both sides of the fracture for sheared intrusions with $\Delta\sigma_n = 1$ MPa and faults.

The slope is increased everywhere for purely opened intrusions. Slope change decreases in amplitude and extension with decreasing $\Delta\sigma_n$. Slope change for sheared intrusions with $\Delta\sigma_n = 1$ MPa or for faults is similar: the slope is increased by the intrusion in the flat summit area, whereas it is decreased on the volcano flanks.

5.2. Subvertical Fractures (α = 80°)

The internal displacement associated with purely opened intrusions and sheared intrusions with large $\Delta\sigma_n$ points normal to the fracture plane (Figure 7). As $\Delta\sigma_n$ decreases, the displacement of sheared intrusions becomes parallel to the fracture plane, pointing upward on the foot side and downward on the hanging side.

At the surface, purely opened intrusions and sheared intrusions with large $\Delta\sigma_n$ show the characteristic bimodal displacement previously described for purely opened intrusions [*Dieterich and Decker*, 1975; *Pollard et al*., 1983] with uplift on both sides of the fracture and subsidence above the fracture. As $\Delta\sigma_n$ decreases, the footwall uplift increases, while the hanging wall starts to subside: sheared intrusions with $\Delta\sigma_n = 1$ MPa and faults are characterized by uplift of the footwall and subsidence of the hanging wall. The horizontal surface displacement corresponding to purely opened intrusions and sheared intrusions with $\Delta\sigma_n \geq 5$ MPa shows opposite displacement, with the footwall moving westward and the hanging wall moving eastward, while the horizontal displacement of sheared intrusions with $\Delta\sigma_n = 1$ MPa and faults is westward on both sides of the fracture.

The slope is increased on the summit and flanks for purely opened intrusions. As $\Delta\sigma_n$ decreases, the extent and amplitude of the slope change increases: slope increases in the summit area and on the footwall and decreases on the hanging side. The slope change of sheared intrusions with $\Delta\sigma_n = 1$ MPa and faults is similar.

6. Systematic Study of Ratios of Surface Displacements

In order to extend the analysis of displacement obtained for two dips (subhorizontal and subvertical) and a stress ratio of $k = 0.6$, we study the displacement associated with a wide range of fracture dips and stress anisotropies. To propose rules of thumb for the determination of the fracture dip and loading from the observed displacement, we follow the approach defined by *Pollard et al*. [1983] and use ratios of maximum surface displacement. By using the ratios, our study becomes dimensionless. We define the ratios of vertical U_z^+/U_z^- and horizontal U_x^+/U_x^- displacements and the ratios of horizontal over vertical displacements for both sides of a fracture U_x^-/U_z^- and U_x^+/U_z^+, where "−" refers to the footwall (subvertical fracture) or head side (subhorizontal fracture), "+" refers to the hanging wall (subvertical fracture) or toe side (subhorizontal fracture) (Figures 3 and 8), and U_z and U_x refer to the maximum vertical and horizontal displacements, respectively. The algorithm used for determining the maximum displacements is explained in Figure S5 in the supporting information. Surface displacement could for instance be provided by InSAR, after retrieving displacement in geographic coordinates [*Wright et al*., 2004; *Samsonov and d'Oreye*, 2012].

In order for the study to be comprehensive, we consider subhorizontal and subvertical fractures with the same mean depth d below the ground surface. This differs from the previous section where subhorizontal and subvertical fractures were assumed to originate from the same depth ($z = 0$). However, the characteristics of fracture stress, displacement, and surface displacement are very close to those found in the previous sections.

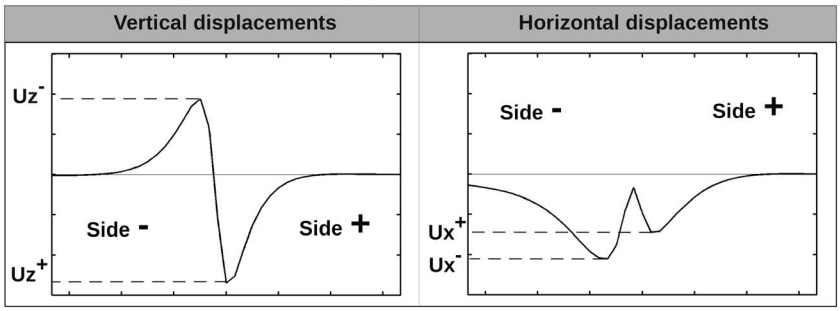

Figure 8. Maximum surface displacement for vertical and horizontal displacements and sides "−" and "+" (see definition in Figure 3). The displacement profiles correspond to a subvertical sheared intrusion with $\Delta\sigma_n = 1$ MPa. Its location is indicated by a dashed line in Figure 7.

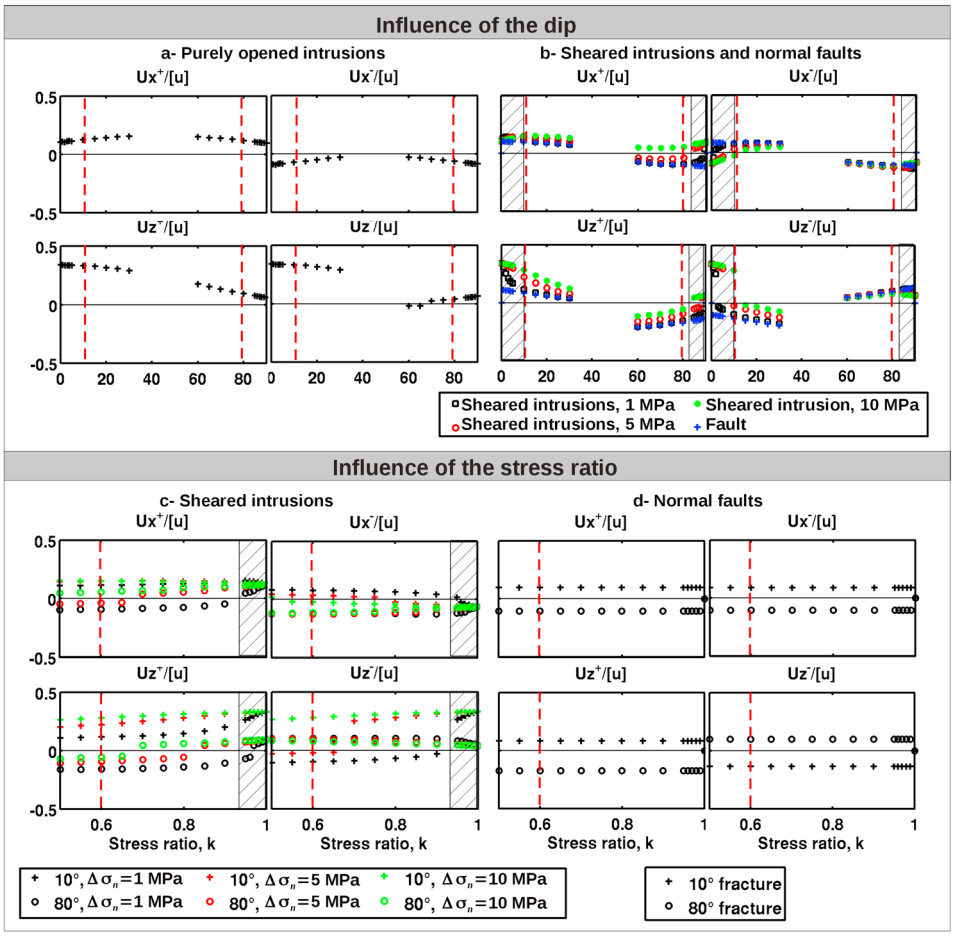

Figure 9. Influence of the fracture dip on maximum surface displacements for different stress changes on the fracture. (a) Influence of the dip for normal stress changes. (b) Influence of the dip for shear and mixed stress changes for several normal stress changes. (c) Influence of the stress ratio for shear stress changes. (d) Influence of the stress ratio for mixed stress changes and several normal stress changes. The fracture length and mean depth are 3 km ($d/l = 1$). Displacements are scaled by $[U]$ given by equation (8). For Figures 9c and 9d, subvertical fractures with an 80° dip and subhorizontal fractures with a 10° dip are considered. For Figures 9b and 9c, the stress ratio is $k = 0.6$. Ratios and signs correspond to the definitions presented in Figures 3 and 8. The red dashed lines correspond to cases presented in Figures 6 and 7. The hatched areas correspond to dips and stress ratios of fractures deforming as purely opened intrusions. Fracture wall interpenetration is prevented.

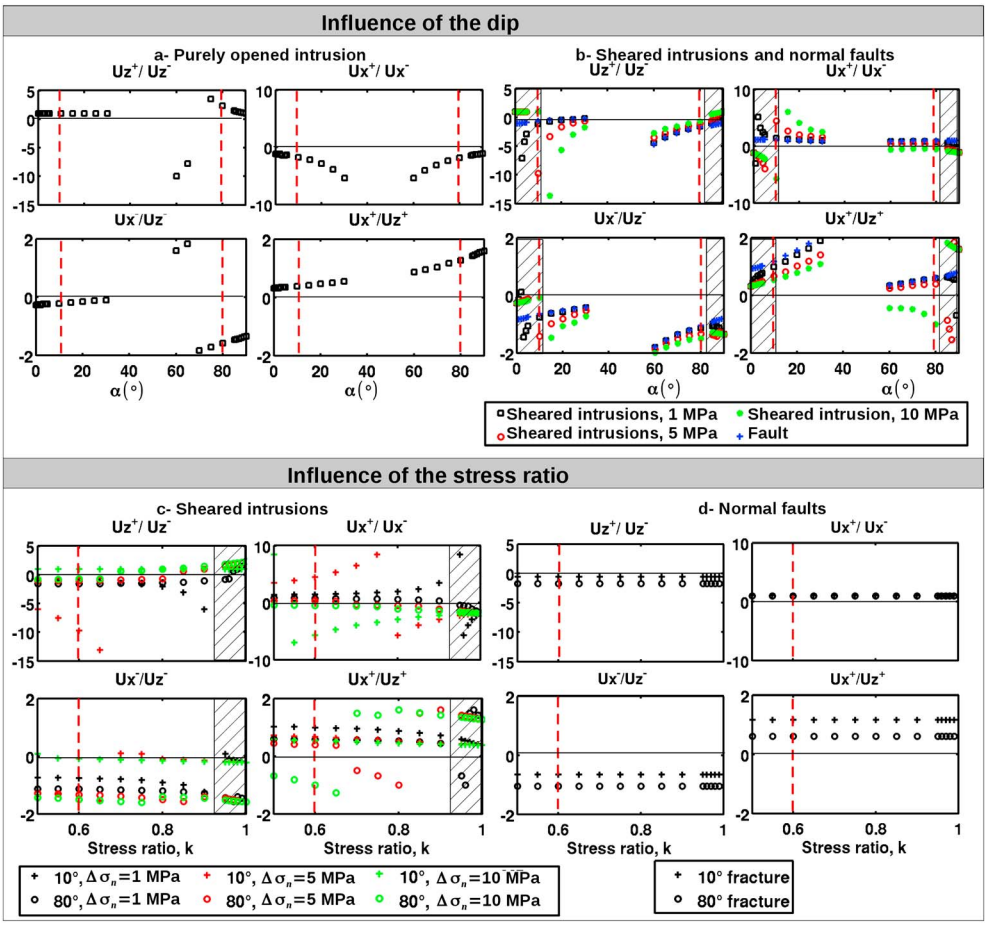

Figure 10. Influence of fracture dip and stress ratio, $k = \sigma_h/\sigma_v$, on ratios of maximum surface displacement for different stress changes on the fracture. (a) Influence of the dip, α, for purely opened sheet intrusions. (b) Influence of α for faults and sheared sheet intrusions with different $\Delta\sigma_n$. Parameter k is fixed at 0.6. (c) Influence of the stress ratio for sheared intrusions with different $\Delta\sigma_n$. (d) Influence of the stress ratio for faults. The mean fracture depth and length are 3 km ($d/l = 1$). For Figures 10c and 10d, a subvertical fracture with $\alpha = 80°$ and a subhorizontal fracture with $\alpha = 10°$ are considered. Signs and ratios correspond to the definitions presented in Figures 3 and 8. The red dashed lines correspond to cases presented in Figures 6 and 7. The hatched areas correspond to dips and stress ratios of fractures deforming as purely opened intrusions. Fracture wall interpenetration is prevented.

6.1. Displacement Ratios as a Function of the Dip, α, and Stress Ratio, k, Taken Separately

The displacement and displacement ratios are computed for subhorizontal fractures ($0° \le \alpha \le 30°$) and subvertical fractures ($60° \le \alpha \le 90°$), using $k = 1$ (purely opened intrusions; Figures 9a and 10a), $k = 0.6$ (sheared intrusions and faults; Figures 9b and 10b), and varying $0.5 \le k \le 1$ for sheared intrusions (Figures 9c and 10c) and faults (Figures 9d and 10d), with fractures at fixed dips of 10° and 80°. Following equation (4), the dips of $\alpha = 0°$ and $\alpha = 90°$ and a stress ratio of $k = 1$ correspond to zero $\Delta\tau$ and thus to zero fault displacement (Figure 9).

We find that for sheared intrusions, surface displacement ratios vary with the dip (Figure 10b), the stress ratio (Figure 10c), and the driving pressure (Figures 10b and 10c). Consequently, their variation has to be studied as a function of these three parameters. However, for faults, normalized displacement, and displacement ratios depend on α (Figures 9b and 10b) but are independent of k (Figures 9d and 10d). Indeed, surface displacement is a linear function of the shear stress, thus k (equation (4)), making the ratio or normalized value independent of k. The consequence is that fault displacement ratios can be studied as a function of the dip alone.

Determination of the dip direction As seen for two particular dips in Figures 6 and 7, we find that for a large range of dips (Figures 10a and 10b), ratios of horizontal over vertical displacements U_x/U_z are negative on side "−" ($U_x^-/U_z^- < 0$) and positive on side "+" ($U_x^+/U_z^+ > 0$), whatever the fracture stress change. The sign of these ratios can thus be used to discriminate the head side/footwall (side "−") from the toe side/hanging

wall (side "+") of fractures, i.e., the dip direction of a fracture. However, there are exceptions to this rule in which ratios on side "+" and on side "−" have the same sign. The first exception is for purely opened intrusions with $60° \leq \alpha \leq 70°$ (Figure 10a), for which U_x^-/U_z^- is positive instead of negative. Indeed, for these dips, the subsidence is greater than the uplift on side "−," a case which does not occur with intrusions that are longer than their height [*Rubin*, 1992]. The second exception is for sheared subvertical intrusions with $\Delta\sigma_n \geq 5$ MPa (Figures 10b and 10c), where U_x^+/U_z^+ is negative instead of positive. These exceptions can be used to discriminate both the stress type and the fracture side. Positive U_x/U_z on both sides are characteristic of purely opened intrusions, whereas negative U_x/U_z on both sides are characteristic of sheared intrusions with $\Delta\sigma_n \geq 5$ MPa. For these purely opened intrusions, side "+" has $U_z > 0$ (Figure 9a), and for the sheared intrusions, sides "+" and "−" have $\left|U_x^+/U_x^-\right| < 1$ (Figure 10b).

Purely opened intrusions versus sheared fractures Sheared intrusions and faults (Figures 10b–10d) have horizontal displacement ratios of U_x^+/U_x^-, which are opposite in signs to those of purely opened intrusions (Figure 10a). Thus, the signs of ratio U_x^+/U_x^- can be used to discriminate purely opened intrusions from sheared intrusions or faults. A fracture with a negative U_x^+/U_x^- is a purely opened intrusion, while one with a positive U_x^+/U_x^- is either a sheared intrusion or a fault. Again, the exception is for sheared intrusions with $\Delta\sigma_n \geq 5$ MPa, $\alpha < 15°$, $\alpha > 85°$ (Figure 10b), and $k > 0.8$ (Figure 10c). As seen before (Figures 6 and 7), these fractures have a surface displacement very similar to those created by purely opened intrusions; thus, in our interpretations, they will be assimilated into purely opened intrusions (dashed areas in Figures 9 and 10).

Faults versus sheared intrusions For sheared intrusions with $\Delta\sigma_n = 1$ MPa, $5° < \alpha < 85°$ (Figure 10b) and $k \leq 0.8$ (Figure 10c) displacement ratios are very close to values determined for faults and will probably be within the measurement error of actual displacement data. Faults and sheared intrusions with $\Delta\sigma_n = 1$ MPa have U_x^+/U_x^- ranging from 1 to 1.2 (Figure 10b). U_x^+/U_x^- is above or below this range for sheared intrusions with $\Delta\sigma_n \geq 5$ MPa.

Determination of the dip After using specific ratios to determine the dip direction and whether a fracture is a purely opened intrusion or a fault/sheared intrusion, we question whether the dip of the fracture can be determined from displacement ratios. For purely opened intrusions, unimodal vertical displacement is obtained for subhorizontal fractures, leading to $U_z^+/U_z^- = 1$ (Figure 10), whereas vertical displacement is bimodal for subvertical fractures. Weakly opened sheared intrusions ($\Delta\sigma_n = 1$ MPa) and faults are characterized by $U_x^+ < 0$ when subhorizontal and $U_x^+ > 0$ when subvertical (Figure 9). For a precise determination of the dip, the ratio U_x^+/U_z^+ can be used, as a given ratio corresponds to a given α (Figure 10a). For sheared intrusions, as displacement ratios vary with α and k (Figures 10b and 10c), the determination of the most relevant displacement ratios will require the study of the joint influence of α and k. For faults (Figure 10b), U_z^+/U_z^-, U_x^-/U_z^-, and U_x^+/U_z^+ can be used for the same reason.

Determination of the driving pressure Displacement ratios vary with $\Delta\sigma_n$. For instance, the greater the $\Delta\sigma_n$, the smaller the U_x^+/U_z^+ and U_x^+/U_z^+. Faults ($\Delta\sigma_n = 0$ MPa) will correspond to the largest U_x^+/U_z^+ and U_x^+/U_z^+.

6.2. Displacement and Displacement Ratios as a Function of the Dip, α, and Stress Ratio, k, Taken Jointly

For sheared intrusions, we intend to generalize the results obtained previously by the systematic study of displacement ratios as a function of α, k, and $\Delta\sigma_n$. Displacement ratios corresponding to purely opened intrusions or faults are not represented as they are independent of the stress ratio. They were described in section 6.1. When a fracture dip is close to 0° and 90°, or the stress field is close to isotropic ($k \sim 1$), $\Delta\tau$ is negligible (equation (4)), and the displacement ratio (Figure 11) becomes similar to the ratio of a purely opened intrusion (Figure 10a).

Determination of the type of fracture We confirm the previous result, indicating U_x^+/U_x^- sign changes when the dip becomes vertical or horizontal or the stress ratio becomes high, corresponding to a fracture becoming purely opened. Thus, the signs of these ratios can be used to discriminate faults/sheared intrusions from purely opened intrusions. Recalling that U_x^+/U_x^- ranges from 1 to 1.2 for sheared intrusions with $\Delta\sigma_n = 1$ MPa or faults (Figures 10b and 10c), we confirm (Figure 11) that the values of $U_x^+/U_x^- > 1.2$ or <1 are specific of purely opened intrusions and sheared intrusions with $\Delta\sigma_n = 1$ MPa.

Determination of the dip, α, the stress ratio, k, and driving pressure, $\Delta\sigma_n$ We confirm that $U_x^- > 0$ and $U_x^- < 0$ are specific to subhorizontal and subvertical faults or sheared intrusions (Figure S6 in the supporting

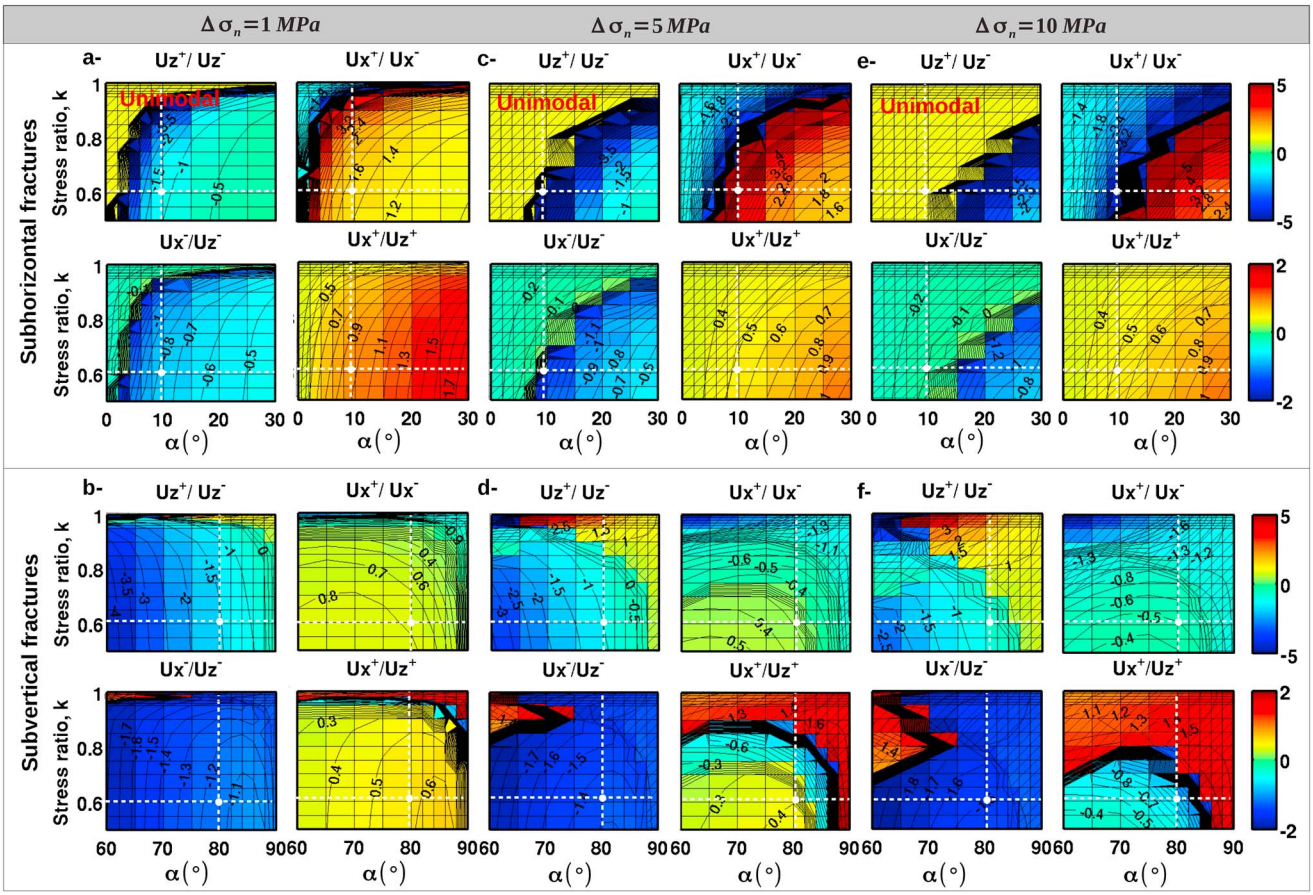

Figure 11. Influence of the fracture dip, α, and stress ratio, $k = \sigma_h/\sigma_v$, on ratios of maximum displacement for sheared sheet intrusions with driving pressure, (a and b) $\Delta\sigma_n = 1$ MPa, (c and d) $\Delta\sigma_n = 5$ MPa, and (e and f) $\Delta\sigma_n = 10$ MPa. Figures 11a, 11c, and 11e show the displacement ratios for subhorizontal fractures. Figures 11b, 11d, and 11f show the displacement ratios for subvertical fractures. The mean fracture depth and length are 3 km ($d/l = 1$). Signs and ratios correspond to the definitions presented in Figures 3 and 8. Horizontal and vertical dashed white lines correspond to stress ratio $k = 0.6$, and dips of 80° and 10°, presented in Figures 10b and 10c, respectively. The intersection of these dashed lines corresponds to models shown in Figures 6 and 7. The hatched areas correspond to fractures with displacement characteristic of purely opened intrusions. Fracture wall interpenetration is prevented.

information), respectively. The isovalues in Figure 11 confirm that the determination of α and k has to be done from several displacement ratios as several combinations of α and k correspond to a given value of the displacement ratio. As all ratios vary with $\Delta\sigma_n$, their combined value also constrains the amplitude of $\Delta\sigma_n$.

6.3. Sensitivity of the Results to the Fracture Length and Depth

Our results were intended to be dimensionless, but because the topography has a characteristic length scale, they also depend, to a small extent, on the fracture depth and length. In order for our results to be robust, those ratios least sensitive to depth and length will be used.

To investigate the influence of the fracture length, displacement ratios (Figures S7–S9 in the supporting information) were computed for fractures half as long ($l = 1.5$ km) and nearly twice as long ($l = 5.4$ km) as our previous calculations ($l = 3$ km). To investigate the influence of the fracture depth (Figures S10–S12 in the supporting information), displacement ratios were computed for a fracture twice as deep ($d = 3$ km below the summit) and nearly half ($d = 1.7$ km) or a third ($d = 1$ km) as deep as our previous calculations ($d = 3$ km). Comparing ratios for the same values of d/l and different lengths and depths (Figures S7 and S10 and Figures S8 and S11 in the supporting information), we find that a first-order approximation showed that ratios depend on d/l. We next investigate how d/l influences the determination of the fracture characteristics and stress anisotropy.

Dip direction For purely opened intrusions, we find that the sign of U_x/U_z remains almost unchanged whatever the fracture length and depth (Figures S7a and S10a in the supporting information). We conclude that the sign of U_x/U_z is a reliable proxy for determining the dip direction. In the same way, $U_z > 0$ remains indicative of side "+" for purely opened intrusions (Figures S7a and S10a in the supporting information), and $\left|U_x^+/U_x^-\right| < 1$ (Figures S8 and S11 in the supporting information) can still be used to discriminate the dip direction of sheared subvertical intrusions.

Type of fracture For all types of fractures, the sign of U_x^+/U_x^- remains unchanged whatever the length and depth (Figures S7a, S8, S10a, and S11 in the supporting information). Therefore, the sign can reliably be used to determine whether an intrusion is purely opened or sheared.

Ratio U_x^+/U_x^- (Figures S8, S7b, S11, and S10b in the supporting information), used to determine whether a fracture is a sheared intrusion or a fault, can be as high as 1.5 for a subhorizontal fault, which is twice as long (Figure S7b in the supporting information) and as low as 0.4 for a subvertical fault at half the depth or one, which is twice as long (Figures S7b and S10b in the supporting information). Thus, we determine that $U_x^+/U_x^- > 1.5$ or < 0.4 are characteristic of sheared intrusions, and that when $0.4 < U_x^+/U_x^- < 1.5$, the fracture can be a sheared intrusion with $\Delta\sigma_n = 1$ MPa or a fault.

Dip, α, stress ratio, k, and driving pressure, $\Delta\sigma_n$ Ratio U_x^+/U_z^+, which we proposed to determine the dip of purely opened intrusions, appears to be a reliable choice as it is little influenced by changes in fracture depth and length (Figures S7a and S10a in the supporting information).

As surface displacement and ratios corresponding to faults are very close to those of sheared intrusions with $\Delta P = 1$ MPa and $k < 0.6$ (Figures 6, 7, and 10b), the same ratios will be used for both types of fracture. For faults and sheared intrusions (Figures S7, S8, S10, and S11 in the supporting information), despite ratios U_z^+/U_z^- and U_x^+/U_z^+ are the least sensitive to variations in the fracture length and depth, ratio U_x^+/U_z^+ is influenced by d/l for $15° < \alpha < 30°$. Therefore, these ratios will give the most reliable dip estimates and will also be able to be used to determine d/l.

6.4. Sensitivity to the Topography

To investigate the influence of the volcano slope, displacement ratios are computed for a flat ground surface and for a steep ground surface with a mean slope of 30° (Figures S13–S16 in the supporting information). We find that whether the topography is flat or steep, we can still use the sign of U_x/U_z, U_z, and the amplitude of $\left|U_x^+/U_x^-\right|$ to determine the "−" and "+" sides of the fracture (Figures S13–S16 in the supporting information).

Similarly, whatever the slope, the sign and the amplitude of U_x^+/U_x^- can be used to discriminate purely opened intrusions from sheared intrusions or faults (Figures S13–S16 in the supporting information). We confirm that ratios $U_x^+/U_x^- > 1.5$ or < 0.4 are specific to sheared intrusions.

The determination of the dip of purely opened intrusions or faults can still be done from U_x^+/U_z^+ Figure S13a in the supporting information), or from U_z^+/U_z^- combined with U_x^+/U_z^+ (Figure S13b in the supporting information), respectively. However, for sheared intrusions, U_z^+/U_z^- and U_x^+/U_z^+ are significantly affected by the mean slope (compare Figures 11a and 11b to Figure S13 in the supporting information). Thus, plots specific to the slopes of the studied volcano (Figure 11 and Figures S16–S18 in the supporting information) should be used to determine α, k, and $\Delta\sigma_n$.

7. Discussion and Case Studies

7.1. Large Flank Displacement

In our models, sheared intrusions lead to fracture shear displacement with the same amplitude as that created by faults, as we have assumed that host rock deviatoric stress is fully relaxed by the fracture movement. In reality, fault displacement is resisted by friction. Although, different types of low-friction slip structures have been suggested on volcanoes, such as pelagic sediments [*Lipman*, 1995], clay-rich sediments, or thermally altered rocks [*Siebert et al*., 1987; *López and Williams*, 1993; *van Wyk de Vries et al*., 2000; *Reid*, 2004; *Cecchi et al*., 2004], which may develop excess hydrostatic pressure [*Dieterich*, 1988; *Day*, 1996; *Thomas et al*., 2004], it is unlikely that full shear stress relaxation occurs on faults. Because magma injections involve null friction, sheared intrusions are the most efficient fractures for flank destabilization. The

influence of a magma intrusion might be enhanced if it is guided by a detachment as the intrusion shear displacement could overcome the frictional resistance of the detachment leading to larger-scale edifice collapse [*Chaput et al*., 2014a].

Lateral flank displacement results from fracture shear displacement. We found that for sheared intrusions, the amount of shear displacement is independent of the amount of opening whatever the proximity of the ground surface and equal to values corresponding to a circular fracture with the same area and stress change embedded in an infinite medium (equation (12)). Consequently, it is a linear function of the fracture length. Our hypothesis on stress orientation (equation (4)) results in maximum shear displacement for sheared intrusions and faults with dips of 30° and 60° and a host rock stress ratio of $k = 0.5$. As shear stresses are assumed to result from the gravitational loading of the edifice, the amplitude of U_s is greater for deeper fractures. Consequently, the largest flank displacement is triggered by the longest, deepest sheared intrusions embedded in a medium with the greatest stress anisotropy (smallest k).

7.2. Application to Flank Failure at the Piton des Neiges Volcano

This study was motivated by the observation of sheared sills in the Salazie Cirque of the Piton des Neiges volcano (Réunion Island: Figure 1). These sills, which act as a detachment, are located on top of a 10 km diameter gabbro and beneath debris avalanche deposits [*Famin and Michon*, 2010; *Chaput et al*., 2014b]. The detachment involved 50–70 sills and stacked into a ~50 m thick pile. In the pile, sills have an average dip of 28°, and their thickness ranges from 0.4 to 1.1 m.

Some of these sills are crosscut by numerous faults, themselves crosscut by more recent sills. This crosscutting relationship indicates that the faults developed during the progressive growth of the sill zone. Using stress inversions of fault slip data, *Chaput et al*. [2014b] found that the stress state within the sill pile alternated between two extreme cases, an extensional and a compressional stress regimes. The observations that faults from the extension are neoformed while faults from the compression are reactivated led the authors to propose that the extension occurred when the deviatoric stress was high, whereas the compression occurred when the deviatoric stress was lower.

We explore the sill shear displacement, U_s, and the driving pressure, $\Delta\sigma_n$, associated with these two contrasting stress regimes. As U_s is insensitive to d/l, it can be directly computed from equation (12). The sills are observed at several outcrops at distances of up to 9 km from the volcano summit. The flow direction, indicated by elongated bubbles, suggests that they probably originate from a source located beneath the summit. Thus, we assume that the sill length l is around 10 km. They are presently located 2.3 km beneath the elevation of Piton des Neiges's summit, but the overburden at the time of their emplacement is estimated to have corresponded to $d = 3.5$ km [*Famin and Michon*, 2010]. We further consider a Young's modulus $E = 50$ GPa, a Poisson's ratio $\nu = 0.25$, and a host rock density of $\rho_r = 2700$ kg/m^3.

When the stress regime was extensional, the sills were oriented at an angle of 28° with respect to the maximum principal stress. As neoformed normal faults crosscut the sills, we estimate that the sills were at the rock strength limit, corresponding to a stress ratio of $0.5 < k < 0.6$ (see section 3.3). Using equation (12), we determine that the shear displacement caused by a sill intrusion was $U_s = 3.7$ m. When the stress regime was compressional, shear displacement should have accommodated the compression. As the contrary is observed and only reactivated faults are observed under this stress regime, we postulate that $k \sim 1$ and that the overpressure induced by the sill was large enough to create a stress permutation. For instance, if the intrusion led to $k = 0.95$, the induced shear displacement was only $U_s = 0.37$ m.

As shown in section 4, the fracture opening depends on the fracture depth over length ratio, d/l. For the pile of sills, we determine that $d/l = 0.4$. Thus, equation (15) and isovalues in Figure S4 in the supporting information have to be used to compute the driving pressure from the observed opening. For sills dipping at 30°, Figure S4a in the supporting information indicates $U_n^* = 0.8$ for $0.5 < k < 0.6$ and $U_n^* = 1.5$ for $k \sim 1$. Considering sill thicknesses ranging from 0.4 to 1.1 m, equation (15) gives driving pressures ranging from $\Delta\sigma_n = 3$ MPa to 8 MPa for $0.5 < k < 0.6$ and $\Delta\sigma_n = 2$ MPa to 5 MPa for $k \sim 1$, consistent with the values assumed for our models and indicating that the model is self-consistent.

We next question whether these sills can trigger large-scale flank displacement. For flank instability to be triggered, either several of the pile sills should be sheared by a small amount, or some of the sills should

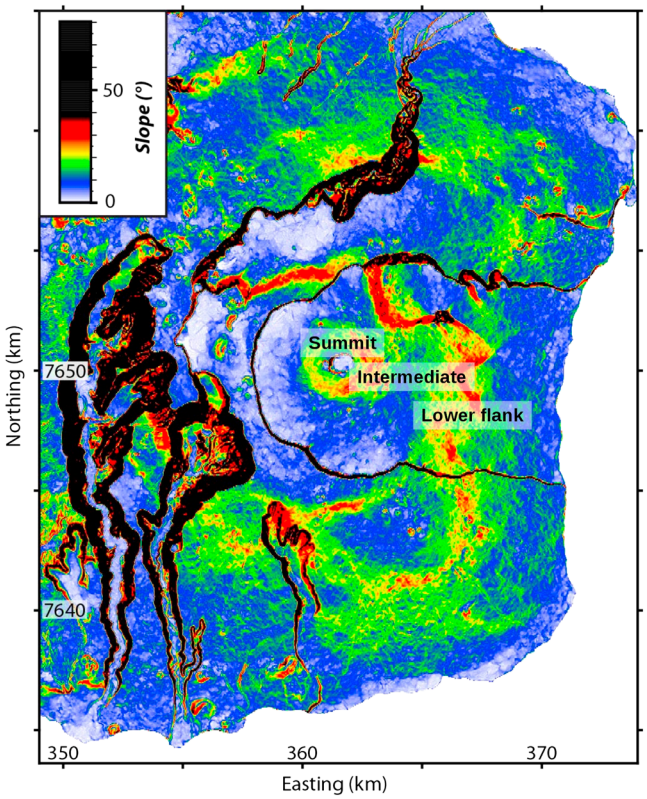

Figure 12. Slope map of Piton de la Fournaise volcano (Réunion Island). The location of this map is indicated in Figure 1. The coordinates are UTM WGS84 (zone 40S).

focus a large amount of the shear displacement. The repetition of shear displacement on parallel sills is problematic. Indeed, in a series of sill intrusions, shear displacement within the first emplaced sill relaxes deviatoric stress along that sill. When a new sill intrudes along previous sills, shear displacement only occurs, provided deviatoric stresses along the sill have been restored, or provided the new intrusion has a different extension so that it crosscuts a different part of the host rock where deviatoric stress have not previously been relaxed.

A mechanism of stress restoration was proposed by *Chaput et al*. [2014b] from the observation of intrusion populations and from the inversion of fault slip data at the volcano. These authors conclude that the alternation of extensional and compressional stress regimes they observe results from stress permutations caused by repeated dikes and sill intrusions. In their model, sill intrusions occur when the maximum principal stress is horizontal and the injected sills are sheared, increasing deviatoric stresses. In a similar way to their model, we propose that shearing of sills diminishes horizontal stress on the head side (Figure 3), allowing new dike intrusions to occur in the nearby N120–140° rift zone, further increasing deviatoric stress along the sill. However, unlike their model, because quasi-isotropic stress only induces a small amount of shear displacement on the sills, we think it more likely that flank instabilities occur when the maximum principal stress is vertical. This could be the case if the intrusion is guided by a preexisting discontinuity, which is the case when the intruded sill is not the first in the pile, or if the sill is not reoriented in response to a stress rotated with respect to the stress in the area where the intrusion initiated [*Maccaferri et al*., 2011]. If all the sills in the pile had been sheared under an extensional stress regime, the series of 50–70 intrusions should have induced 180–260 m of lateral flank displacement. The trigger of a debris avalanche, such as the one associated with the deposits observed on top of the sill zone, cannot be explained by this model alone, but would require the emplacement of sills along a detachment crosscutting the whole volcano, as well as a weak zone beneath the volcano summit, as suggested by the recent study of *Chaput et al*. [2014a].

7.3. Influence of the Different Types of Fractures on the Slopes of Basaltic Volcanoes

It has long been thought that one of the main morphological features of basaltic volcanoes is the presence of a gentle and uniform slope [*Simkin and Seibert*, 1994]. More recent studies show that a steep slope is more common than expected on basaltic edifices [*Rowland and Garbeil*, 2000; *Naumann and Geist*, 2000; *Michon and Saint-Ange*, 2008]. Volcanoes like those in the Western Galapagos Islands [*Rowland*, 1996; *Mouginis-Mark et al*., 1996; *Rowland and Garbeil*, 2000], Karthala (Grand Comore) [*Rowland and Garbeil*, 2000), or Piton de la Fournaise (Réunion Island) [*Rowland and Garbeil*, 2000; *Michon and Saint-Ange*, 2008] share similar flank slope patterns. The lower part of the flanks have a typical basaltic shield gentle slope (8 to 15°), followed by a steep slope locally reaching 35 to 40° at intermediate elevations, and a very low slope (less than 5°) in their summit area.

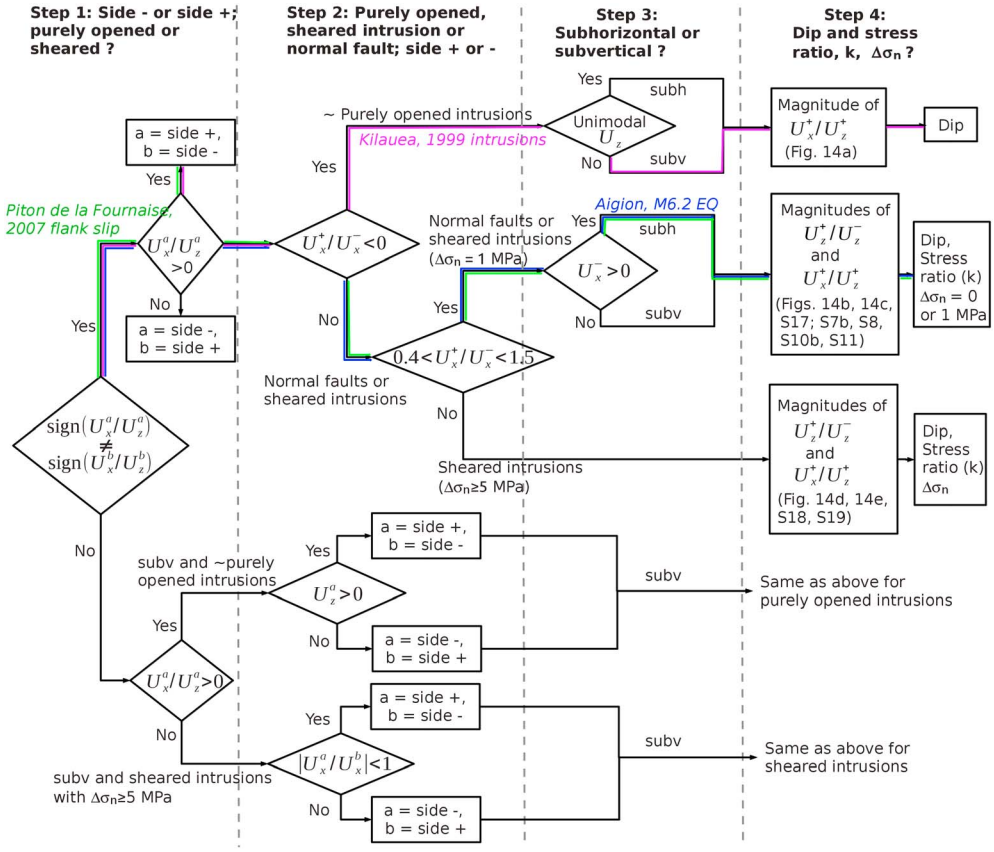

Figure 13. Flow chart indicating the steps of the decision tree to determine the fracture and host rock characteristics from ratios of maximum surface displacements. Side "−" refers to the foot side (subvertical fracture) or head side (subhorizontal fracture), and side "+" refers to the hanging side (subvertical fracture) or toe side (subhorizontal fracture) (Figures 3 and 8). Subv stands for subvertical fracture and subh for subhorizontal fracture. The magenta lines show the determination path for the fracture associated with the Kilauea 1999 intrusion, the blue lines show this path for the *M* 6.2 Aigion earthquake, and the green lines correspond to the April 2007 Piton de la Fournaise eruption.

A previous study attributed the elevated steep slope at intermediate elevations on the Piton de la Fournaise summit cone to the repetition of subvertical magma injections in N25–30° and N120° rift zones [*Michon et al.*, 2009]. The fact that this steep slope is circumferential (Figure 12) remains unexplained. The April 2007 eruptions and models of slope change induced by fractures (Figure 6) suggest that the emplacement of subhorizontal fractures beneath the east flank could provide an alternative explanation for the observed steep slope. Indeed, subhorizontal fractures increase the slope at the summit and intermediate elevations, but shear displacement of these fractures decreases the slope around the summit area, producing a ring of increased slope at intermediate elevations.

7.4. Determination of Fracture Characteristics and Host Rock Stress Ratio From Surface Displacement Ratios

A four-step procedure is proposed to guide the determination of the type of fracture (purely opened, sheared intrusion, or normal fault), the fracture dip direction, dip, the host rock stress ratio, *k*, and the driving pressure, $\Delta\sigma_n$. It is summarized as a decision tree (Figure 13). Recall that this decision tree applies to buried fractures with $0° < \alpha < 30°$ and $60° < \alpha < 90°$, mainly loaded by gravity.

1. In step 1, the location of side "−" and side "+" of the fracture is determined from the sign of the ratio U_x/U_z. Negative U_x/U_z values are characteristic of side "−," while positive U_x/U_z values are characteristic of side "+" (Figure 10). If U_x/U_z has the same sign on both sides and U_x/U_z is positive, the fracture is a purely opened subvertical intrusion. If this sign is negative on both sides, the fracture is a subvertical sheared intrusion with $\Delta\sigma_n \geq 5$ MPa.

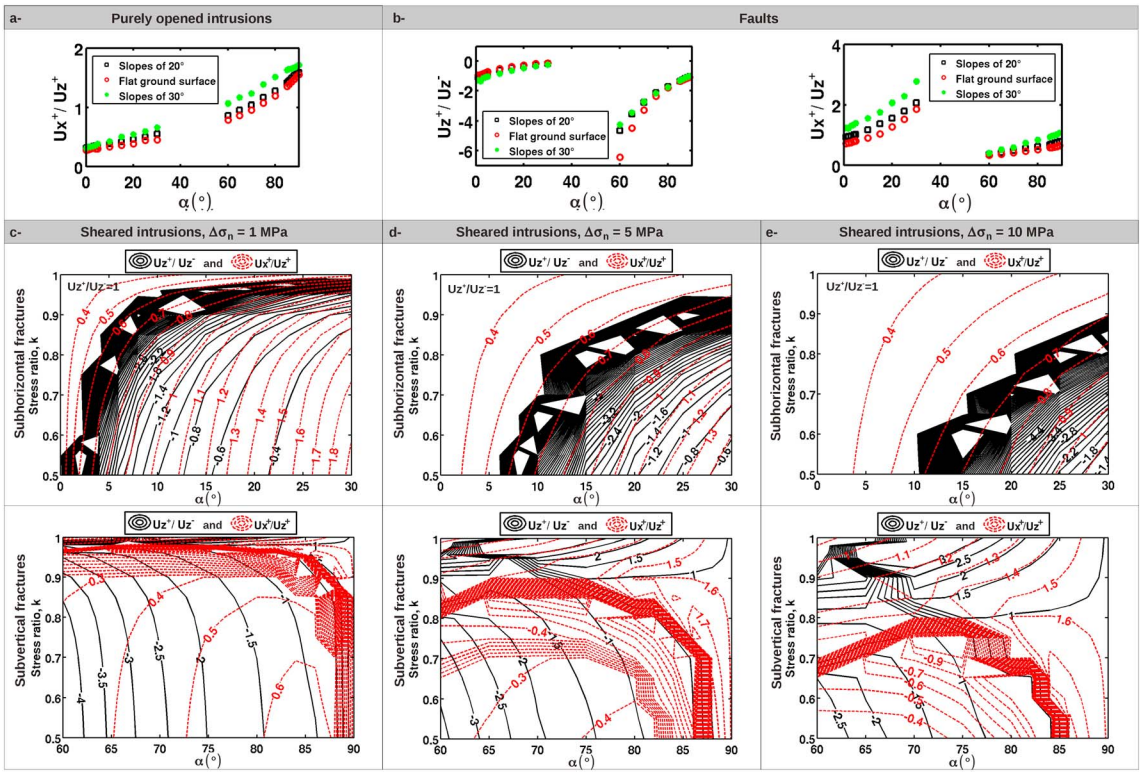

Figure 14. Displacement ratios used to determine the dip and type of fracture, as well as the host rock stress anisotropy. (a) Ratio U_x^+/U_z^+ is used for purely opened sheet intrusions when the mean slopes of the volcano of have values of 0°, 20°, and 30°. (b) Ratios for faults ($\Delta\sigma_n = 0$ MPa) on volcanoes with mean slopes of 0°, 20°, and 30°. (c) Combined ratios for sheared intrusions with $\Delta\sigma_n = 1$ MPa. (d) Combined ratios for sheared intrusions with $\Delta\sigma_n = 5$ MPa. (e) Combined ratios for sheared intrusions with $\Delta\sigma_n = 10$ MPa. The mean fracture depth and length are 3 km ($d/l = 1$). Ratios U_z^+/U_z^- and U_x^+/U_z^+ in Figures 14b–14e are used jointly for faults or sheared sheet intrusions. In Figures 14c–14e, volcanoes have 20° slopes. Signs and ratios correspond to the definitions presented in Figures 3 and 8.

2. In step 2, if sides "+" and "−" have been determined in step 1, then the fracture type is determined from U_x^+/U_x^-. When $U_x^+/U_x^- < 0$ shear stress change is negligible and the fracture is behaving like a purely opened intrusion, we can go directly to step 3 to determine whether it is subvertical or subhorizontal. When $U_x^+/U_x^- > 0$, the fracture is either a fault or a sheared intrusion. If $U_x^+/U_x^- > 1.5$ or $U_x^+/U_x^- < 0.4$, the fracture is a sheared intrusion; otherwise, it is not possible to distinguish a fault from a sheared intrusion with $\Delta\sigma_n = 1$ MPa (Figure 10b and Figure 11). If sides "+" and "−" have not been determined in step 1 and if $U_x/U_z > 0$ on both sides, side "+" is the side where $U_z > 0$. If $U_x/U_z < 0$ on both sides, sides "+" and "−" will be such that $\left|U_x^+/U_x^-\right| < 1$.
3. In step 3, we determine whether a fracture is subhorizontal or subvertical, except for sheared intrusions with $\Delta\sigma_n \geq 5$MPa for which we can go directly to step 4. Purely opened intrusions have characteristic unimodal U_z, whereas faults or sheared intrusions have positive U_x^-.
4. In step 4, the dip of purely opened intrusions is determined from U_x^+/U_z^+ for the specific slope of the studied volcano (Figure 14a). The greater U_x^+/U_z^+, the greater the dip. For faults and sheared intrusions with $\Delta\sigma_n = 1$ MPa, α is determined from the combination of U_z^+/U_z^- and U_x^+/U_z^+ given in Figures 14b and 14c and Figure S17 in the supporting information for volcanoes with slopes of 0°, 20°, or 30°. It is generally not possible to distinguish faults from sheared intrusions with $\Delta\sigma_n = 1$ MPa (Figure 10b), with some exceptions corresponding to $k > 0.7$ and to subhorizontal fractures with $20° < \alpha < 30°$ and $d/l \leq 0.6$ (Figures S7b, S9, S10b, and S12 in the supporting information), for which the largest U_x^+/U_z^+ correspond to faults. For sheared intrusions such that $\Delta\sigma_n \geq 5$ MPa, combined ratios given in Figures 14d ($\Delta\sigma_n = 5$ MPa) and 14e ($\Delta\sigma_n = 10$ MPa) should be used to determine α, $\Delta\sigma_n$, and k when the volcano slope is 20°, whereas Figures S18 ($\Delta\sigma_n = 5$ MPa) or S19 ($\Delta\sigma_n = 10$ MPa) in the supporting information should be used when volcano slopes are 0° or 30°. The stress change of purely opened intrusions and faults cannot be determined as displacement ratios are independent of them.

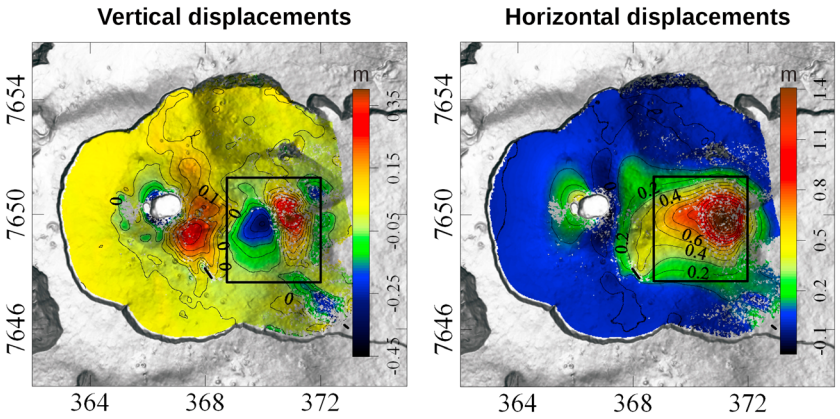

Figure 15. Displacement associated with the 2007 eruption. This displacement was computed from two Envisat and three ALOS interferograms [modified from *Clarke et al*., 2013]. The black box indicates the area for which ratios of displacements are computed. The coordinates are UTM WGS84 (zone 40S).

To illustrate the use of the decision tree, it is applied to two examples, which have already been analyzed using combinations of uniform dislocation models [*Okada*, 1985, 1992] and inversions. One example concerns the 1999 east rift zone East Rift Zone Kilauea intrusion, the other concerns the *M* 6.2 1995 Aigion (Greece) earthquake. The 1999 Kilauea intrusion was captured by campaign GPS, continuous GPS, leveling data, and InSAR data [*Cervelli et al*., 2002]. However, to show the simple applicability of the decision tree, we only use the available continuous GPS and leveling data. Continuous GPS data indicate maximum values of horizontal displacements of $U_x^{\text{north}} = -0.06$ m north of the rift zone and $U_x^{\text{south}} = 0.102$ m south of the rift. Vertical displacements measured along a north-south road crossing Kilauea upper east rift zone were considered with respect to the southernmost leveling station as it is the furthest from the rift; thus, the least affected by the 1999 intrusion. We get $U_z^{\text{north}} = 0.04$ m and $U_z^{\text{south}} = 0.055$ m. Successive steps (Figure 13) are the following: U_x/U_z being positive to the south, the fracture is dipping south, and side "+" is to the south. As $U_x^+/U_x^- < 0$, the fracture is a purely opened intrusion, and as U_z is bimodal, the intrusion is subvertical. The dip is determined to be 90° from $U_x^+/U_z^+ = 1.85$ using Figure 14a. As the reference for vertical displacements is probably in an area affected by the rift intrusion, it is likely that U_z^+ is larger and that the dip is below 90°. The obtained characteristics are consistent with the 80° steep south dipping dike obtained by *Cervelli et al*. [2002].

To analyze displacements associated with the *M* 6.2 Aigion earthquake, we use campaign GPS measurements corrected from their secular trend [*Bernard et al*., 1997]. Maximum horizontal displacements are $U_x^{\text{north}} = 0.08$ m and $U_x^{\text{south}} = 0.04$ m, and maximum vertical displacements are $U_z^{\text{north}} = 0.04$ m and $U_z^{\text{south}} = -0.15$ m. The steps followed are indicated on Figure 13. As U_x/U_z is positive to the north, the fracture is dipping north: side "−" is to the north. As U_x^+/U_x^- is positive, the fracture is a fault, and as $U_x^- > 0$, the fracture is subhorizontal. Now computing $U_z^+/U_z^- = -0.27$ and $U_x^+/U_z^+ = 2$ and using Figure 14b, we determine a dip of 30°, close to the 35° dip determined by *Bernard et al*. [1997].

7.5. Determination of the Characteristics of the Fracture Associated With the 2007 Flank Displacement at Piton de la Fournaise Volcano

Between 2 April and 1 May 2007, a major eruptive crisis occurred at Piton de la Fournaise volcano, Réunion Island (Figure 1), characterized by its largest emitted magma volumes of the 20th and 21st centuries and by a 300 m deep caldera collapse at the summit. Ground displacement associated with this eruption was measured by interferograms from the Envisat and ALOS satellites. Two Envisat and three ALOS interferograms were used simultaneously following the procedure outlined by *Wright et al*. [2004] to retrieve maps of the vertical and horizontal displacements that occurred during the eruption [*Clarke et al*., 2013]. These maps evidence complex displacement patterns, resulting from several events: the intrusion of a dike into the volcano rift zones, the collapse of the summit caldera, and an eastward displacement of the

volcano's eastern flank of up to 1.4 m (Figure 15). After the eruption, the displacement of the east flank continued at a decreasing rate for more than a year [*Augier*, 2011].

We use the strategy outlined above (section 7.4) to characterize the fracture associated with the eastward displacement of the eastern flank. Measured maximum vertical displacements have the following values: $U_z^{west} = -0.45$ m, $U_z^{east} = 0.35$ m, while the horizontal displacement is unimodal so that $U_x^{west} = U_x^{east} = 1.4$ m. For the first step (chart in Figure 13), we calculate $U_x^{west}/U_z^{west} = -3.1$ m and $U_x^{east}/U_z^{east} = 4$ m. As U_x/U_z is negative to the west and positive to the east, the eastern flank corresponds to side "+," indicating that the fracture is dipping east. The second step requires the calculation of the ratio U_x^+/U_x^-, which is $U_x^+/U_x^- = 1$. As $0.4 < U_x^+/U_x^- < 1.5$, the fracture is either a fault or a sheared intrusion with $\Delta\sigma_n = 1$ MPa. For the third step, ratios $U_z^+/U_z^- = -0.8$ and $U_x^+/U_z^+ = 4$ are determined. The large U_x^+/U_z^+ value is indicative of a subhorizontal fracture with a small $\Delta\sigma_n$ and a small d/l. In our simulations, 25° dip faults ($\Delta\sigma_n = 0$ MPa) with $d/l = 0.3$, $d = 3$ km, and $l = 9$ km (Figure S7b in the supporting information) give values of $U_x^+/U_z^+ = 3.4$ and $U_z^+/U_z^- = -0.25$, close to values determined for the 2007 eruption. The corresponding preliminary model is shown in Figure S20 in the supporting information.

Three possible explanations can be given to account for the discrepancies between simulated and observed displacement ratios:

1. The fracture causing the east flank displacement has a d/l value lower than the lowest d/l tested ($d/l = 0.3$). A study of the posteruptive east-flank displacement associated with the eruption [*Augier*, 2011] showed that the flank displacement corresponds to the closing of a 4 km long quadrangular fracture located 400 m beneath the ground surface. This fracture has a $d/l = 0.1$. As the coeruptive east flank displacement is probably induced by the same shallow fracture as the post eruptive displacement, this hypothesis is likely.
2. The fracture shape is more complex than a planar square. Planar surfaces are favorable geometries for faulting, but the fracture area undergoing stress change might be more complex than a square. Again, preliminary models for the posteruptive displacements [*Augier*, 2011] favor trapezoidal fractures with their base to the east.
3. The measured displacement does not solely result from a single source. On Piton de la Fournaise east flank, InSAR recorded displacement resulting from several events—a dike intrusion in the rift zones and a collapse of the summit caldera [*Froger et al*., 2014].

For this event, the different measured ratios could not be reconciled using the step-by-step Cartesian approach determined in this study. To refine the study and determine the complex fracture depth, shape, and stress change, a numerically formal inversion has to be performed considering that the source might be a sheared intrusion, in the same way as in the study of *Hooper et al*. [2011] at Kverkfjoll volcano.

8. Conclusions

Our study uses 3-D numerical models to investigate the ability of a variety of volcano fractures to trigger flank displacement and flank instability. We model fracture and surface displacement for two groups of fracture orientations, determined from field studies at oceanic shield volcanoes: shallow sheet intrusions (depths less than 1 km) that are mostly subvertical with dips ranging from 60° to 90°, and deep sheet intrusions (depths greater than 1 km) that are mainly subhorizontal with dips ranging from 0° to 30°. To make our study comprehensive, we consider the three different types of fracture that occur on volcanoes: (i) purely opened intrusions are fractures submitted to normal stress changes, (ii) sheared intrusions are fractures submitted to both normal and shear stress changes, and (iii) faults are fractures submitted to shear stress changes. Assuming that the stress field is anisotropic and shear displacement occurs on fractures that are not emplaced normal to a principal stress, we explore the influence of host rock stress anisotropies, characterized by stress ratios $0.5 \leq k = \sigma_h/\sigma_v \leq 1$, where low k corresponds to a state of failure equilibrium and $k = 1$ corresponds to a state of lithostatic equilibrium.

As our model assumes full stress relaxation, sheared intrusions undergo the same amount of shear stress change as faults. In nature, fault displacement is resisted by friction, so that faults are unable to fully relax shear stresses. On the contrary, the injection of magma cancels friction, leading to a full shear stress

relaxation, making sheared intrusions the most efficient slip medium on a volcano. We find that for faults and sheared intrusions, the shear displacement on fractures is proportional to the applied stress change and fracture surface and is independent of the proximity to the ground surface, so that it can be computed from the analytic solution corresponding to a circular fracture with the same area as the study fracture embedded in an infinite medium. Consequently, the largest flank displacement is triggered by the longest, deepest, fractures dipping closest to 45° in a medium with the highest stress anisotropy.

For sheared and purely opened intrusions, the amount of opening is largely influenced by the ground surface. Intrusions with intermediate dips of $30° < \alpha < 80°$ open less than intrusions in an infinite medium, whereas subhorizontal and subvertical intrusions can open up to 4 times more. At shallow depth, the occurrence of shear displacement induces fracture closure, resulting in sheared intrusions undergoing less opening than purely opened intrusions.

Our models may be used in two ways. At first, forward approach is to compute the shear displacement on a pile of sills exposed by erosion at Piton des Neiges volcano (Réunion Island). Using this forward approach, we estimated that each of the sills intruded caused a 3.7 m shear displacement. Assuming that the deviatoric stress along the sills is restored by dike intrusions occurring in an associated rift zone, we further estimate that the 50 m high sill pile might have incrementally induced 180–260 m of lateral flank displacement.

Alternatively, it is also possible to use our models in a reverse approach to determine the characteristics of a fracture and the host rock stress anisotropy from the pattern of the surface displacement. Using the fact that displacement can be described as a continuum from purely opened intrusions through sheared intrusions to faults, with a progressive decrease in driving pressure, we extend the approach *Pollard et al*. [1983] developed for purely opened subvertical intrusions to characterize a variety of fractures. We systematically study the influence of the stress ratio, k, and fracture orientations on ratios of maximum surface displacements on both sides of a fracture, which might be located beneath topographies with slopes of 0, 20°, or 30°. From the analysis of signs and amplitudes of these ratios, we have developed a deterministic step-by-step procedure (represented as a decision tree) to determine the fracture type (purely opened, sheared intrusion, or fault), dip, the host rock stress anisotropy, and the driving pressure. This procedure provides a priori models which can be used to infer bounds to the parameter space before it is explored through a formal inversion.

Applying this procedure to the 1.4 m high coeruptive flank displacement on Piton de la Fournaise (Réunion Island) in April 2007, we find that this displacement might have been caused by a 25° east dipping subhorizontal fault, rather than a sheared intrusion, with a depth over length ratio smaller than 0.3. The inability of the method to fully reconcile the observed ratios might result from a too simplistic model or from the east flank displacement containing contributions of other events that took place at the time of the InSAR data acquisition—a rift dike intrusion and a summit caldera collapse.

Appendix A: Solving 3-D Boundary Element Subject to the Condition That Normal Displacement Is Positive

Boundary element method codes involving fractures imply the resolution of a linear system verifying the prescribed boundary conditions. Solving this linear system may lead to solutions where fracture interpenetration occurs. However, most geological and geophysical applications call for solutions where fracture wall interpenetration is prevented. Mathematically, this condition results in displacement inequality constraints.

The linear system to solve for the mixed 3-D boundary element method [*Cayol*, 1996] used in this study is written as

$$\boldsymbol{AX} = \boldsymbol{R}, \tag{A1}$$

where $\boldsymbol{A}$ is the influence coefficient matrix for displacements $\boldsymbol{U} = (\boldsymbol{u}^1 \,..\boldsymbol{u}^{n_L})^T$ for n_L massive elements and displacement discontinuities $\boldsymbol{D} = (\boldsymbol{d}^1 \,..\boldsymbol{d}^{n_F})^T$ for n_F fracture elements, with $\boldsymbol{d}^k = (d_1^k d_2^k d_3^k)$ the displacement discontinuity vector at the k^{th} element; $\boldsymbol{X} = (\boldsymbol{U} \quad \boldsymbol{D})^T$ is the vector of unknown displacements and displacement discontinuities; and R is a known vector which takes the applied boundary tractions into account.

To avoid fracture interpenetration, normal displacement must be positive, which corresponds to the following inequality constraint for $l = 1,.., n_F$:

$$\boldsymbol{d}^l \boldsymbol{n}^l > 0, \tag{A2}$$

where $\boldsymbol{n}^l = \left(n_1^l n_2^l n_3^l\right)$ is the normal to the l^{th} element.

Boundary element methods usually address this problem using a penalty method [*Crouch et al*., 1983; *Cooke and Pollard*, 1997], where it is assumed that fractures are filled with a stiff material, which resists fracture closure. With this method the solution can fail to converge or be wrong [*Mijar and Arora*, 2000]. Instead, we use a method where the inequality constraint is enforced through Lagrange multipliers. Namely, we use an augmented Lagrangian with block relaxation technique. In order to implement this method, the system (A1) has to be reformulated into a minimization problem. Here the matrix A is invertible but not symmetric. To obtain a symmetric system, we write the following system, equivalent to (A1)

$$\boldsymbol{A}^T \boldsymbol{A} \boldsymbol{X} = \boldsymbol{A}^T \boldsymbol{R}. \tag{A3}$$

Solution of this system corresponds to the minimization of the function

$$J(\boldsymbol{X}) = \frac{1}{2} \boldsymbol{X}^T \boldsymbol{A}^T \boldsymbol{A} \boldsymbol{X} - \boldsymbol{R}^T \boldsymbol{A} \boldsymbol{X}. \tag{A4}$$

If there are no constraints, the minimization has to be done over n_{dof}, where $n_{\text{dof}} = n_F + n_L$. Here we add the constraint (A2) which can easily be rewritten in terms of $\boldsymbol{X}$ as

$$\boldsymbol{N} \boldsymbol{X} \leq 0, \tag{A5}$$

where $\boldsymbol{N}$ is a matrix with n_F rows and n_{dof} columns. We then consider the problem of the minimization of the function J defined by (A4) under the constraints (A5). Minimization is performed through a variant of the augmented Lagrangian method, based on the introduction of a fictitious vector variable $\boldsymbol{Y}$ in n_F, which takes into account the sign constraints (A5), and the following function [see, for example, *Fortin and Glowinski*, 1983]

$$L(\boldsymbol{X}, \boldsymbol{Y}, \boldsymbol{\lambda}) = J(\boldsymbol{X}) + I(\boldsymbol{Y}) + \boldsymbol{\lambda}^T (\boldsymbol{N} \boldsymbol{X} - \boldsymbol{Y}) + \frac{r}{2} \|\boldsymbol{N} \boldsymbol{X} - \boldsymbol{Y}\|_{n_F}^2. \tag{A6}$$

where $\lambda \in n_F$ is the Lagrange multiplier of the constraints (A5), $r > 0$ is the augmentation parameter, and the function I is defined as

$$I(\boldsymbol{Y}) = \begin{cases} 0, & \text{if} \quad \boldsymbol{Y} \leq 0 \\ +\infty, & \text{otherwise} \end{cases}. \tag{A7}$$

In practice, one does not need to compute this function explicitly, but it is used in the computation of the optimality conditions. The Kuhn–Karush–Tucker optimality conditions for constrained optimization problems [see *Fortin and Glowinski*, 1983] lead to the following iterative algorithm:

1. Initialization: choose $\boldsymbol{X}^{(0)} \in n_{\text{dof}}$, $\boldsymbol{Y}^{(0)} \in n_F$, and $\boldsymbol{\lambda}^{(0)} \in n_F$ at iteration number $k \geq 0$, $(\boldsymbol{X}^{(k)}, \boldsymbol{Y}^{(k)}, \boldsymbol{\lambda}^{(k)})$ being known:
2. Compute $\boldsymbol{X}^{(k+1)}$ minimizing $L(\boldsymbol{X}, \boldsymbol{Y}^{(k)}, \boldsymbol{\lambda}^{(k)})$;
3. Compute $\boldsymbol{Y}^{(k+1)}$ minimizing $L(\boldsymbol{X}^{(k)}, \boldsymbol{Y}, \boldsymbol{\lambda}^{(k)})$;
4. Update the Lagrange multiplier : $\boldsymbol{\lambda}^{(k+1)} = \boldsymbol{\lambda}^{(k)} + r(\boldsymbol{N} \boldsymbol{X}^{(k+1)} - \boldsymbol{Y}^{(k+1)})$.

The first step leads to the solution of a linear system of the same dimension as (A1) but with a different matrix. The second step then does lead to an explicit expression. Moreover the initial vector $\boldsymbol{X}^{(0)}$ can be set as the solution of the original unconstrained problem (A1), and if it satisfies the constraints (A5), no iteration needs to be performed.

Appendix B: Stress Changes Applied to Magma-Filled Fractures

When magma is injected into the host rock considered as an elastic medium, stress perturbations along the fracture surface are assumed to result from the difference between the magma pressure and stresses in the edifice. The stress perturbation matrix is defined as

$$\Delta \boldsymbol{\sigma}(x, y, z) = \begin{bmatrix} P_m(z) - k\sigma_{\text{v}}(x, y, z) & 0 & 0 \\ 0 & P_m(z) - k\sigma_{\text{v}}(zx, y) & 0 \\ 0 & 0 & P_m(z) - \sigma_{\text{v}}(x, y, z) \end{bmatrix}, \tag{B1}$$

where the magma pressure $P_m(z)$ is induced by the magma density ρ_m, and the magma pressure ΔP_0:

$$P_m(z) = -\rho_m g z + \Delta P_0. \tag{B2}$$

We assume fractures are far enough from the ground surface for the maximum principal stress to be vertical, and we assume that σ_v corresponds to the weight of the overlying rocks:

$$\sigma_v(x,y,z) = \rho_r g\,[z_{surf}(x,y) - z]. \tag{B3}$$

where $z_{surf}(x,y)$ is the elevation of the surface above each point of the fracture.

Magma pressure is considered to be greater than the magnitude of the maximum principal stress so that fractures of any orientation can dilate. Changes of normal and shear stresses ($\Delta\sigma_n(x,y,z)$ and $\Delta\tau(x,y,z)$, respectively), resolved on a fracture dipping at an angle α, with unit normal vector $n = (\sin(\alpha), 0, \cos(\alpha))^T$, are computed from the stress tensor given in equation (B1) as

$$\Delta\sigma_n(x,y,z) = P_m(z) - \sigma_v(x,y,z)\left[k\sin(\alpha)^2 + \cos(\alpha)^2\right], \tag{B4}$$

and

$$\Delta\tau(x,y,z) = \sigma_v(x,y,z)(k-1)\cos(\alpha)\sin(\alpha). \tag{B5}$$

This shear stress change assumes that host rock stresses are fully relaxed by fracture movements.

Practically, in our boundary element code, a mean stress vector $\overline{T}$ is applied to the fracture,

$$\overline{T} = \overline{\Delta\sigma(x,y,z)}\,n \tag{B6}$$

where $\Delta\sigma(x,y,z)$ is the stress tensor in equation (B1).

To compute the mean stress vector $\overline{T}$, we determine the value of ΔP_0 such that the mean normal stress change $\overline{\Delta\sigma_n(x,y,z)}$ (further noted $\Delta\sigma_n$) equals a given value.

The mean shear stress change, $\overline{\Delta\tau(x,y,z)}$ (further noted $\Delta\tau$), is derived from equation (B5) and has the value

$$\Delta\tau = \rho_r g d(k-1)\cos(\alpha)\sin(\alpha), \tag{B7}$$

where $d = (\overline{z}_{surf} - \overline{z}_{frac})$ is the mean fracture depth below the ground surface, with $\overline{z}_{surf}$ the mean elevation of the ground surface above the fracture, and $\overline{z}_{frac}$ the mean fracture elevation (Figure 3).

Appendix C: Mean Fracture Displacement Induced by Normal and Shear Stress Changes on Circular Fractures in an Infinite Medium

Net opening and shear displacement for a flat circular plane fracture, of radius a, submitted to a uniform stress change follow elliptical profiles [*Eshelby*, 1957; *Segall*, 2010]. Their values differ depending on whether the stress change is a driving pressure $\Delta\sigma_n$ or a shear stress change $\Delta\tau$,

$$u_n(r) = \frac{4}{\pi}\frac{(1-\nu^2)}{E}a\Delta\sigma_n\sqrt{1-\frac{r^2}{a^2}}, \tag{C1}$$

and

$$u_s(r) = \frac{8}{\pi}\frac{(1-\nu^2)}{E(2-\nu)}a\Delta\tau\sqrt{1-\frac{r^2}{a^2}}. \tag{C2}$$

Computation of the mean crack displacement requires the evaluation of

$$U_n = \overline{u_n(r)} = \frac{4}{\pi^2}\frac{(1-\nu^2)}{E}\frac{1}{a}\Delta\sigma_n\int_0^{2\pi}\int_0^a r\sqrt{1-\frac{r^2}{a^2}}\,dr d\theta, \tag{C3}$$

and

$$U_s = \overline{u_s(r)} = \frac{8}{\pi^2}\frac{(1-\nu^2)}{E(2-\nu)}\frac{1}{a}\Delta\tau\int_0^{2\pi}\int_0^a r\sqrt{1-\frac{r^2}{a^2}}\,dr d\theta. \tag{C4}$$

With $\int_0^a r\sqrt{1-\frac{r^2}{a^2}}\,dr = \frac{a^3}{3}$, equations (C3) and (C4) become

$$U_s = \frac{32}{3\pi}\frac{(1-\nu^2)}{E(2-\nu)}\frac{a}{2}\Delta\tau, \tag{C5}$$

and

$$U_n = \frac{16}{3\pi}\frac{(1-\nu^2)}{E}\frac{a}{2}\Delta\sigma_n. \tag{C6}$$

Acknowledgments

This research was supported by the INSU-CNRS ALEAS program and by the Laboratory of Excellence Clervolc (contribution 91). The PhD fellowship of T. Catry was funded by the VINCI program of the French Italian University. The field data of Piton des Neiges were collected by M. Chaput during her PhD funded by the French Ministère de la Recherche et de l'Enseignement Supérieur. The data used for Figure 2b are part of M. Chaput Doctorat Thesis, accessible through the HAL repository site, http://hal.archives-ouvertes.fr/. We thank V. Pinel and T. Walter for a review of an early version of this paper as well as G. Currenti and an anonymous reviewer for their careful and thoughtful reviews. We also thank Francesca van Wyk de Vries for proofreading the manuscript for english grammar and spelling.

References

Ancochea, E., J. L. Brändle, M. J. Huertas, F. Hernán, and R. Herrera (2008), Dike-swarms, key to the reconstruction of major volcanic edifices: The basic dikes of La Gomera (Canary Islands), *J. Volcanol. Geotherm. Res.*, *173*(3), 207–216.

Anderson, E. M. (1938), The dynamics of sheet intrusion, *Proc. R. Soc. Edinburgh*, *58*, 242–251.

Augier, A. (2011), Etude de l'éruption d'Avril 2007 du Piton de la Fournaise (île de la Réunion) à partir de données d'interférométrie RADAR et GPS, développement et application de procédures de modélisation, PhD thesis, Lab. Magmas et Volcans, Univ. Blaise Pascal, Clermont-Ferrand, France.

Beauducel, F., and F. H. Cornet (1999), Collection and three-dimensional modeling of GPS and tilt data at Merapi volcano, Java, *J. Geophys. Res.*, *104*(B1), 725–736.

Bernard, P., et al. (1997), The Ms= 6.2, June 15, 1995 Aigion earthquake (Greece): Evidence for low angle normal faulting in the Corinth rift, *J. Seismolog.*, *1*(2), 131–150.

Borgia, A. (1994), Dynamic basis of volcanic spreading, *J. Geophys. Res.*, *99*(B9), 17,791–17,804, doi:10.1029/94JB00578.

Borgia, A., L. Ferrari, and G. Pasquarè (1992), Importance of gravitational spreading in the tectonic and volcanic evolution of Mount Etna, *Nature*, *357*(6375), 231–235.

Cayol, V. (1996), *Analyse Élastostatique Tridimensionnelle du Champ de Déformations des Édifices Volcaniques par Éléments Frontières Mixtes*, Doctorat, Univ. de Paris VII, Paris, France.

Cayol, V., and F. H. Cornet (1997), 3D mixed boundary elements for elastostatic deformation field analysis, *Int. J. Rock Mech. Min. Sci.*, *34*(2), 275–287.

Cayol, V., and F. H. Cornet (1998), Three-dimensional modeling of the 1983–1984 eruption at Piton de la Fournaise Volcano, Réunion Island, *J. Geophys. Res.*, *103*(B8), 18,025–18,037, doi:10.1029/98JB00201.

Cayol, V., J. H. Dieterich, A. T. Okamura, and A. Miklius (2000), High magma storage rates before the 1983 eruption of Kilauea, Hawaii, *Science*, *288*(5475), 2343–2346.

Cecchi, E., B. V. W. de Vries, and J. M. Lavest (2004), Flank spreading and collapse of weak-cored volcanoes, *Bull. Volcanol.*, *67*(1), 72–91.

Cendrero, A. (1970), The volcano-plutonic complex of La Gomera (Canary Islands), *Bull. Volcanologique*, *34*(2), 537–561.

Cervelli, P. F., and A. Miklius (2003), The shallow magmatic system of Kïlauea Volcano, *U.S. Geol. Surv. Prof. Pap.*, *1676*, 149.

Cervelli, P., P. Segall, F. Amelung, H. Garbeil, C. Meertens, S. Owen, A. Miklius, and M. Lisowski (2002), The 12 September 1999 upper east rift zone dike intrusion at Kilauea volcano, Hawaii, *J. Geophys. Res.*, *107*(B7), ECV 3-1–ECV 3-13, doi:10.1029/2001JB000602.

Chadwick, W. W., Jr., and J. H. Dieterich (1995), Mechanical modeling of circumferential and radial dike intrusion on Galapagos volcanoes, *J. Volcanol. Geotherm. Res.*, *66*(1), 37–52.

Chaput, M., V. Pinel, V. Famin, L. Michon, and J.-L. Froger (2014a), Cointrusive shear displacement by sill intrusion in a detachment: A numerical approach, *Geophys. Res. Lett.*, *41*, 1937–1943, doi:10.1002/2013GL058813.

Chaput, M., V. Famin, and L. Michon (2014b), Deformation of basaltic shield volcanoes under cointrusive stress permutations, *J. Geophys. Res. Solid Earth*, *119*, 274–301, doi:10.1002/2013JB010623.

Chevallier, L., and N. Vatin-Perignon (1982), Volcano-structural evolution of Piton des Neiges, Reunion Island, Indian Ocean, *Bull. Volcanologique*, *45*(4), 285–298.

Clarke, D., F. Brenguier, J. L. Froger, N. M. Shapiro, A. Peltier, and T. Staudacher (2013), Timing of a large volcanic flank movement at Piton de la Fournaise Volcano using noise-based seismic monitoring and ground deformation measurements, *Geophys. J. Int.*, *195*(2), 1132–1140.

Cooke, M. L., and D. D. Pollard (1997), Bedding-plane slip in initial stages of fault-related folding, *J. Struct. Geol.*, *19*(3), 567–581.

Crouch, S. L., A. M. Starfield, and F. J. Rizzo (1983), Boundary element methods in solid mechanics, *J. Appl. Mech.*, *50*, 704.

Currenti, G., and C. A. Williams (2014), Numerical modeling of deformation and stress fields around a magma chamber: Constraints on failure conditions and rheology, *Phys. Earth Planet. Inter.*, *226*, 14–27.

Currenti, G., C. Del Negro, G. Ganci, and C. Williams (2008), Static stress changes induced by the magmatic intrusions during the 2002-2003 Etna eruption, *J. Geophys. Res.*, *113*, B10206, doi:10.1029/2007JB005301.

Dahm, T. (2000), Numerical simulations of the propagation path and the arrest of fluid-filled fractures in the earth, *Geophys. J. Int.*, *141*(3), 623–638.

Day, S. J. (1996), Hydrothermal pore fluid pressure and the stability of porous, permeable volcanoes, *Geol. Soc. London Spec. Publ.*, *110*(1), 77–93.

Delaney, P. T., D. D. Pollard, J. I. Ziony, and E. H. McKee (1986), Field relations between dikes and joints: Emplacement processes and paleostress analysis, *J. Geophys. Res.*, *91*(B5), 4920–4938, doi:10.1029/JB091iB05p04920.

Di Muro, A., N. Métrich, D. Vergani, M. Rosi, P. Armienti, T. Fougeroux, E. Deloule, I. Arienzo, and L. Civetta (2014), The shallow plumbing system of Piton de la Fournaise Volcano (La Réunion Island, Indian Ocean) revealed by the major 2007 Caldera-Forming eruption, *J. Petrol.*, *55*(7), 1287–1315, doi:10.1093/petrology/egu025.

Dieterich, J. H. (1988), Growth and persistence of Hawaiian volcanic rift zones, *J. Geophys. Res.*, *93*(B5), 4258–4270, doi:10.1029/JB093iB05p04258.

Dieterich, J. H., and R. W. Decker (1975), Finite element modeling of surface deformation associated with volcanism, *J. Geophys. Res.*, *80*(29), 4094–4102, doi:10.1029/JB080i029p04094.

Dieterich, J., V. Cayol, and P. Okubo (2000), The use of earthquake rate changes as a stress meter at Kilauea volcano, *Nature*, *408*(6811), 457–460.

Elsworth, D., and S. J. Day (1999), Flank collapse triggered by intrusion: the Canarian and Cape Verde Archipelagoes, *J. Volcanol. Geotherm. Res.*, *94*(1), 323–340.

Eshelby, J. D. (1957), The determination of the elastic field of an ellipsoidal inclusion, and related problems, *Proc. R. Soc. London, Ser. A*, *241*(1226), 376–396.
Famin, V., and L. Michon (2010), Volcano destabilization by magma injections in a detachment, *Geology*, *38*(3), 219–222.
Fernández, C., J. de la Nuez, R. Casillas, and E. García Navarro (2002), Stress fields associated with the growth of a large shield volcano (La Palma, Canary Islands), *Tectonics*, *21*(4), 13–1, doi:10.1029/2000TC900038.
Fortin, M., and R. Glowinski (1983), *Augmented Lagrangian Methods*, Studies in Mathematics and its Applications, 15, Amsterdam.
Froger, J. L., Y. Fukushima, P. Briole, T. Staudacher, T. Souriot, and N. Villeneuve (2004), The deformation field of the August 2003 eruption at Piton de la Fournaise, Reunion Island, mapped by ASAR interferometry, *Geophys. Res. Lett.*, *31*, L14601, doi:10.1029/2004GL020479.
Froger, J. L., V. Cayol, and V. Famin (2014), The March-April 2007 eruption of Piton de la Fournaise as recorded by interferometric data, in *Active Volcanoes of the Southwest Indian Ocean: Piton de la Fournaise and Karthala*, Active Volcanoes of the World, edited by P. Bachèlery et al., Springer, Berlin and Heidelberg.
Fukushima, Y., V. Cayol, and P. Durand (2005), Finding realistic dike models from interferometric synthetic aperture radar data: The February 2000 eruption at Piton de la Fournaise, *J. Geophys. Res.*, *110*, B03206, doi:10.1029/2004JB003268.
Fukushima, Y., V. Cayol, P. Durand, and D. Massonnet (2010), Evolution of magma conduits during the 1998–2000 eruptions of Piton de la Fournaise volcano, Réunion Island, *J. Geophys. Res.*, *115*, B10204, doi:10.1029/2009JB007023.
Holcomb, R. T., and R. C. Searle (1991), Large landslides from oceanic volcanoes, *Mar. Georesour. Geotechnol.*, *10*(1–2), 19–32.
Hooper, A., B. Ófeigsson, F. Sigmundsson, B. Lund, P. Einarsson, H. Geirsson, and E. Sturkell (2011), Increased capture of magma in the crust promoted by ice-cap retreat in Iceland, *Nat. Geosci.*, *4*(11), 783–786.
Iverson, R. M. (1995), Can magma-injection and groundwater forces cause massive landslides on Hawaiian volcanoes?, *J. Volcanol. Geotherm. Res.*, *66*(1), 295–308.
Jaeger, J. C., N. G. Cook, and R. Zimmerman (2009), *Fundamentals of Rock Mechanics*, John Wiley, London, U. K.
Kavanagh, J. L., T. Menand, and R. S. J. Sparks (2006), An experimental investigation of sill formation and propagation in layered elastic media, *Earth Planet. Sci. Lett.*, *245*(3), 799–813.
Keating, B. H., and W. J. McGuire (2000), Island edifice failures and associated tsunami hazards, *Pure Appl. Geophys.*, *157*(6–8), 899–955.
Kelfoun, K., T. Giachetti, and P. Labazuy (2010), Landslide-generated tsunamis at Réunion Island, *J. Geophys. Res.*, *115*, F04012, doi:10.1029/2009JF001381.
Letourneur, L., A. Peltier, T. Staudacher, and A. Gudmundsson (2008), The effects of rock heterogeneities on dyke paths and asymmetric ground deformation: The example of Piton de la Fournaise (Réunion Island), *J. Volcanol. Geotherm. Res.*, *173*(3), 289–302.
Lipman, P. W. (1995), Declining growth of Mauna Loa during the last 100,000 years: Rates of lava accumulation vs. gravitational subsidence, *Geophys. Monogr. Ser.*, *92*, 45–80.
López, D. L., and S. N. Williams (1993), Catastrophic volcanic collapse: relation to hydrothermal processes, *Science*, *260*(5115), 1794–1796.
Lundgren, P., F. Casu, M. Manzo, A. Pepe, P. Berardino, E. Sansosti, and R. Lanari (2004), Gravity and magma induced spreading of Mount Etna volcano revealed by satellite radar interferometry, *Geophys. Res. Lett.*, *31*, L04602, doi:10.1029/2003GL018736.
Maccaferri, F., M. Bonafede, and E. Rivalta (2011), A quantitative study of the mechanisms governing dike propagation, dike arrest and sill formation, *J. Volcanol. Geotherm. Res.*, *208*(1), 39–50.
Marinoni, L. B., and A. Gudmundsson (2000), Dykes, faults and palaeostresses in the Teno and Anaga massifs of Tenerife (Canary Islands), *J. Volcanol. Geotherm. Res.*, *103*(1), 83–103.
Menand, T. (2008), The mechanics and dynamics of sills in layered elastic rocks and their implications for the growth of laccoliths and other igneous complexes, *Earth Planet. Sci. Lett.*, *267*(1), 93–99.
Menand, T. (2011), Physical controls and depth of emplacement of igneous bodies: A review, *Tectonophysics*, *500*(1), 11–19.
Merle, O., and A. Borgia (1996), Scaled experiments of volcanic spreading, *J. Geophys. Res.*, *101*(B6), 13,805–13,817, doi:10.1029/95JB03736.
Michon, L., and F. Saint-Ange (2008), Morphology of Piton de la Fournaise basaltic shield volcano (La Réunion Island): Characterization and implication in the volcano evolution, *J. Geophys. Res.*, *113*, B03203, doi:10.1029/2005JB004118.
Michon, L., V. Cayol, L. Letourneur, A. Peltier, N. Villeneuve, and T. Staudacher (2009), Edifice growth, deformation and rift zone development in basaltic setting: Insights from Piton de la Fournaise shield volcano (Réunion Island), *J. Volcanol. Geotherm. Res.*, *184*(1–2), 14–30.
Mijar, A. R., and J. S. Arora (2000), Review of formulations for elastostatic frictional contact problems, *Struct. Multi. Optim.*, *20*(3), 167–189.
Moore, J. G., D. A. Clague, R. T. Holcomb, P. W. Lipman, W. R. Normark, and M. E. Torresan (1989), Prodigious submarine landslides on the Hawaiian Ridge, *J. Geophys. Res.*, *94*(B12), 17,465–17,484, doi:10.1029/JB094iB12p17465.
Mouginis-Mark, P. J., S. K. Rowland, and H. Garbeil (1996), Slopes of western Galapagos volcanoes from airborne interferometric radar, *Geophys. Res. Lett.*, *23*(25), 3767–3770, doi:10.1029/96GL03280.
Naumann, T., and D. Geist (2000), Physical volcanology and structural development of Cerro Azul Volcano, Isabela Island, Galápagos: Implications for the development of Galápagos-type shield volcanoes, *Bull. Volcanol.*, *61*(8), 497–514.
Okada, Y. (1985), Surface deformation due to shear and tensile faults in a half-space, *Bull. Seismol. Soc. Am.*, *75*(4), 1135–1154.
Okada, Y. (1992), Internal deformation due to shear and tensile faults in a half-space, *Bull. Seismol. Soc. Am.*, *82*(2), 1018–1040.
Papatheodorou, G., and G. Ferentinos (1997), Submarine and coastal sediment failure triggered by the 1995, $M_s = 6.1$ R Aegion earthquake, Gulf of Corinth, Greece, *Mar. Geol.*, *137*(3), 287–304.
Peltier, A., T. Staudacher, and P. Bachèlery (2007), Constraints on magma transfers and structures involved in the 2003 activity at Piton de La Fournaise from displacement data, *J. Geophys. Res.*, *112*, B03207, doi:10.1029/2006JB004379.
Peltier, A., V. Famin, P. Bachèlery, V. Cayol, Y. Fukushima, and T. Staudacher (2008), Cyclic magma storages and transfers at Piton de La Fournaise volcano (La Réunion hotspot) inferred from deformation and geochemical data, *Earth Planet. Sci. Lett.*, *270*(3), 180–188.
Pollard, D. D., and G. Holzhausen (1979), On the mechanical interaction between a fluid-filled fracture and the Earth's surface, *Tectonophysics*, *53*(1), 27–57.
Pollard, D. D., P. T. Delaney, W. A. Duffield, E. T. Endo, and A. T. Okamura (1983), Surface deformation in volcanic rift zones, *Tectonophysics*, *94*(1), 541–584.
Prôno, E., J. Battaglia, V. Monteiller, J. L. Got, and V. Ferrazzini (2009), P-wave velocity structure of Piton de la Fournaise volcano deduced from seismic data recorded between 1996 and 1999, *J. Volcanol. Geotherm. Res.*, *184*(1), 49–62.
Reid, M. E. (2004), Massive collapse of volcano edifices triggered by hydrothermal pressurization, *Geology*, *32*(5), 373–376.
Roeloffs, E. (1996), Poroelastic techniques in the study of earthquake-related hydrologic phenomena, *Adv. Geophys.*, *37*, 135–195.
Rowland, S. K. (1996), Slopes, lava flow volumes, and vent distributions on Volcan Fernandina, Galapagos Islands, *J. Geophys. Res.*, *101*(B12), 27,657–27,672, doi:10.1029/96JB02649.
Rowland, S. K., and H. Garbeil (2000), Slopes of oceanic basalt volcanoes, in *Remote Sensing of Active Volcanism*, edited by P. J. Mouginis-Mark, J. A. Crisp, and J. H. Fink, pp. 223–247, AGU, Washington, D. C.

Rubin, A. M. (1992), Dike-induced faulting and graben subsidence in volcanic rift-zones, *J. Geophys. Res.*, *97*, 1839–1858, doi:10.1029/91JB02170.

Samsonov, S., and N. d'Oreye (2012), Multidimensional time-series analysis of ground deformation from multiple InSAR data sets applied to Virunga Volcanic Province, *Geophys. J. Int.*, *191*, 1095–1108, doi:10.1111/j.1365-246X.2012.05669.x.

Segall, P. (2010), *Earthquake and Volcano Deformation*, Princeton Univ. Press, Princeton, N. J.

Segall, P., J. R. Grasso, and A. Mossop (1994), Poroelastic stressing and induced seismicity near the Lacq gas field, southwestern France, *J. Geophys. Res.*, *99*(B8), 15,423–15,438, doi:10.1029/94JB00989.

Segall, P., E. K. Desmarais, D. Shelly, A. Miklius, and P. Cervelli (2006), Earthquakes triggered by silent slip events on Kīlauea volcano, Hawaii, *Nature*, *442*(7098), 71–74.

Siebert, L., H. Glicken, and T. Ui (1987), Volcanic hazards from Bezymianny-and Bandai-type eruptions, *Bull. Volcanol.*, *49*(1), 435–459.

Simkin, T., and L. Seibert (1994), *Volcanoes of the World*, 2nd ed., Geoscience, Tucson, Ariz.

Staudigel, H., and H. U. Schmincke (1984), The Pliocene seamount series of La Palma/Canary Islands, *J. Geophys. Res.*, *89*(B13), 11,195–11,215, doi:10.1029/JB089iB13p11195.

Stein, R. S., G. C. King, and J. Lin (1992), Change in failure stress on the southern San Andreas fault system caused by the 1992 magnitude = 7.4 Landers earthquake, *Science*, *258*(5086), 1328–1332.

Swanson, D. A., W. A. Duffield, and R. S. Fiske (1976), Displacement of the south flank of Kilauea Volcano: The result of forceful intrusion of magma into the rift zones: Interpretation of geodetic and geologic information leads to a new model for the structure of Kilavea Volcano, *U.S. Geol. Surv. Prof. Pap.*, *963*.

Takada, Y., and Y. Fukushima (2013), Volcanic subsidence triggered by the 2011 Tohoku earthquake in Japan, *Nat. Geosci.*, *6*(8), 637–641.

Thomas, M. E., N. Petford, and E. N. Bromhead (2004), The effect of internal gas pressurization on volcanic edifice stability: Evolution towards a critical state, *Terra Nova*, *16*(5), 312–317.

Tibaldi, A. (2003), Influence of cone morphology on dykes, Stromboli, Italy, *J. Volcanol. Geotherm. Res.*, *126*(1), 79–95.

Tilling, R. I., and J. J. Dvorak (1993), Anatomy of a basaltic volcano, *Nature*, *363*(6425), 125–133.

Townend, J., and M. D. Zoback (2000), How faulting keeps the crust strong, *Geology*, *28*(5), 399–402.

Tryggvason, E. (1986), Multiple magma reservoirs in a rift zone volcano: Ground deformation and magma transport during the September 1984 eruption of Krafla, Iceland, *J. Volcanol. Geotherm. Res.*, *28*(1), 1–44.

van Wyk De Vries, B. V. W., and P. W. Francis (1997), Catastrophic collapse at stratovolcanoes induced by gradual volcano spreading, *Nature*, *387*(6631), 387–390.

van Wyk De Vries, B. V. W., N. Kerle, and D. Petley (2000), Sector collapse forming at Casita volcano, Nicaragua, *Geology*, *28*(2), 167–170.

Walker, G. P. (1986), Koolau Dike Complex, Oahu: Intensity and origin of a sheeted-dike complex high in a Hawaiian volcanic edifice, *Geology*, *14*(4), 310–313.

Walker, G. P., and P. R. Eyre (1995), Dike complexes in American Samoa, *J. Volcanol. Geotherm. Res.*, *69*(3), 241–254.

Watanabe, T., T. Masuyama, K. Nagaoka, and T. Tahara (2002), Analog experiments on magma-filled cracks: Competition between external stresses and internal pressure, *Earth Planets Space*, *54*(12), 1247–1262.

Wright, T. J., B. E. Parson, and Z. Lu (2004), Toward mapping surface deformation in three dimensions using InSAR, *Geophys. Res. Let.*, *31*, L01607, doi:10.1029/2003GL018827.

Yun, S., P. Segall, and H. Zebker (2006), Constraints on magma chamber geometry at Sierra Negra Volcano, Galápagos Islands, based on InSAR observations, *J. Volcanol. Geotherm. Res.*, *150*(1), 232–243.

Zbinden, E. A., and J. M. Sinton (1988), Dikes and the petrology of Waianae Volcano, Oahu, *J. Geophys. Res.*, *93*(B12), 14,856–14,866, doi:10.1029/JB093iB12p14856.